Properties, Fabrication and Applications of Plasmonic Semiconductor Nanocrystals

Journal:	*Catalysis Science & Technology*
Manuscript ID	CY-MRV-12-2019-002511.R1
Article Type:	Minireview
Date Submitted by the Author:	09-Mar-2020
Complete List of Authors:	Yin, Haibo; Osaka University, Division of Materials and Manufacturing Science Kuwahara, Yasutaka; Osaka University, Graduate School of Engineering, Division of Materials and Manufacturing Science Mori, Kohsuke; Osaka University, Division of Materials and Manufacturing Science Louis, Catherine; UPMC, Laboratoire de réactivité de Surface Yamashita, Hiromi; Osaka University, Division of Materials and Manufacturing Science

REVIEW

Properties, Fabrication and Applications of Plasmonic Semiconductor Nanocrystals

Haibo Yin,[a] Yasutaka Kuwahara,[abc] Kohsuke Mori,[ab] Catherine Louis[d] and Hiromi Yamashita*[ab]

Received 00th January 20xx,
Accepted 00th January 20xx

DOI: 10.1039/x0xx00000x

In semiconductor nanocrystals (NCs), a new regime has been opened in plasmonic field since the discovery of localized surface plasmon resonances (LSPRs). LSPRs that lead to near-field enhancement, scattering, and resonant absorption around the NC can be tuned in the range from visible to near-infrared (NIR) region across a wide optical spectral by synthetically varying doping level, and post synthetically *via* electrochemical control, photochemical control, and chemical oxidation and reduction. In this review, we will focus on the three widely explored and interrelated examples and their manipulation methods of LSPR of (1) hydrogen molybdenum bronzes (H_xMoO_{3-y}) NCs, (2) hydrogen tungsten bronzes (H_xWO_{3-y}) NCs, and (3) oxygen vacancy doped molybdenum tungsten oxide ($Mo_xW_{1-x}O_{3-y}$) NCs. Finally, a brief outlook toward applications of these plasmonic NCs are presented.

1. Introduction

The glass of the colored glazed cup, preserved in Nara national museum in Japan from the eighth century, has different colors of transmission and reflection, which is a very classic early example of a dichroic material. The dichroic properties of this artifact derive from plasmonic metal nanoparticles (NPs) embedded in the glass, which shows what we now know as plasmonic effect. Prior to that, our knowledge of localized surface plasmon resonance of metal NPs, especially silver (Ag) and gold (Au), has been preliminarily established, which most often lie in the visible spectra range.[1-5] As a frontier in material, what remains now are questions about how LSPRs are different in nanocrystals (NCs) of the semiconductor.[4-9] With a better understanding of free carrier properties in semiconductors and the advances in colloidal synthesis, the properties of metal-like LSPRs in a variety of NCs material classes have been actively explored, including silicon, metal nitrides, metal chalcogenides, and metal oxides.[8-12] For example, Zhao and co-workers firstly reported that $Cu_{2-x}S$ NCs exhibit strong LSPR in the near infrared (NIR) region in 2009.[8] Soon after, Luther et al. demonstrated that appreciable free carrier concentration in semiconductor NCs is a prerequisite for sustaining LSPRs, which can be reached from the visible through the terahertz region by relying on the doping level and the size of the nanostructure.[4] Due to plasmonic absorption, all the above NCs show strong resonances in the NIR region. For metal NPs (such as Ag and Au), the natural resonance frequencies for LSPRs induced by the high charge concentration (around 10^{22} cm^{-3}) usually appear in the visible region. Complex morphologies and large size of NPs cause the plasmonic absorption to lie in the NIR or mid-infrared (MIR) region.[13-20] On the contrary, the carrier concentration (10^{19}-10^{21} cm^{-3}) of semiconductor NCs can be tuned *via* electrochemical reactions, photochemical, chemical doping, and postsynthetic chemical reactions.[21-30] A modification of the copper to sulfide stoichiometry indeed impacts the LSPRs peak position as shown by Zhao et al.. Analogously, charge carriers that result in plasmonic response in NIR can be generated by nonstoichiometric composition in WO_{3-x} and in $Cu_{3-x}P$ nanocrystals. Even some samples with simple shapes and sizes less than 50 nm, variation of their carrier concentration still allows for a controlled LSPR tuning in a wide optical range.

The origin of LSPRs in semiconductors NCs is the key point of this review. The dielectric function or material's complex polarizability determines the response of a conductive medium to the incident light.[4,5] The dielectric function involves the movement of free carriers, excitation of vibrational modes, and the contribution from transitions between electronic bands, which mainly describes the bulk properties of a material.[31,32] Among them, the concentration of the free carriers and characteristics (such as crystal structure and band structure) contribute to the dielectric function.[32-35] These encompass the intrinsic properties of the material. The nature of light-matter interactions should be considered from the geometrical features of NCs and the dielectric properties of the surrounding medium standpoint. For example, in thin films, the frequency and angle of the incident light have a significant influence on the oscillation of electronic charge, which usually results in strong LSPRs at the air-metal interface.

The plasmonic properties of semiconductor NCs rely largely on dopant concentration, dopant type, and shape and size of NCs.[36,37] The effective design of plasmonic semiconductor NCs

---

[a] *Division of Materials and Manufacturing Science, Graduate School of Engineering, Osaka University, Osaka, 565-0871, Japan.*
[b] *Unit of Elements Strategy Initiative for Catalyst & Batteries (ESICB), Kyoto University, Kyoto, 615-8245, Japan.*
[c] *JST, PRESTO, 4-1-8 HonCho, Kawaguchi, Saitama, 332-0012, Japan.*
[d] *Sorbonne Universités, UPMC Univ Paris 06, UMR CNRS 7197, Laboratoire de Réactivité de Surface, 4 Place Jussieu, Tour 43-33, 3ème étage, Case 178, F-75252 Paris, France.*

usually has three powerful ways: (1) control the size and shape of the NCs in conjunction, (2) select reasonable dopant types, (3) increase the concentration of the free carrier by increasing activated dopant concentration. Of course, so far a few important breakthroughs for making LSPR assignments have been made by preciously controlling the intrinsic dopant and geometric properties of NCs during colloidal synthesis.

(1) **Size and Shape Dependence:** The control of nucleation and growth is an essential prerequisite of nanocrystals synthesis, which determines the final composition, uniformity, and size and shape of the NCs. Establishment of macroscopic thermodynamic (such as concentration and temperature) can realize the above control, which of course also involves microscopic chemical considerations such as ionic size, valence of metal precursors, ligand binding strengths, and precursor reactivities.[38-40] Swiart et al. prepared high-quality plasmonic $Cu_{2-x}Se$ NCs with controlled size ranging from 7.2 to 16.5 nm by using OAm-Se and OA-Se precursors, where nucleation is initiated at suitable temperature.[41] Subsequently, the optimization of growth of $Cu_{2-x}Se$ NCs is conducted by aging the colloidal dispersion for a time. Colloidal $Cu_{2-x}Te$ nanoplates, nanocubes, nanorods, and nanospheres were also synthesized by regulating the concentrations of Cu and Te precursors and the reaction temperature.[42, 43] Diffusion-limited growth occurs after nucleation stage, which only lasts for a short time in the early stages of crystallization. Hutchison et al. reported that the size and structure of indium oxide NCs can be governed at a subnanometer scale by slow addition of indium carboxylate precursor into hot oleyl alcohol. During the above NCs synthesis process, the growth of existing cores is impeded and new nucleation occurs.[43-45] In addition, the surfactants in colloidal synthesis acts as capping ligands (such as halogens and organic ligands) to balance surface charges and passivate dangling bonds at NC surface by shape control, which allows NCs to show LSPR at the shorter wavelengths in the NIR region.[46,47] Shape control is not limited to the considerations of thermodynamic and kinetic, but also can be achieved in more complicated case of doped NCs.[48,49] Depending on the bonding strength and steric effect of ligand (oleic acid), dot-shaped CdTe NCs with relatively broad size distribution can be prepared. Based on the principles of nucleation and growth, the synthesis of NCs can be controlled by selecting appropriate synthetic methods such as solvothermal, colloidal, nonthermal plasma methods and so forth. Introducing defects (impurities or vacancies) can make plasmonic among of host materials (e.g., metal oxides and metal chalcogenides).[50-53] Knoll et al. prepared tetrapod-shaped ZnO NCs with the ultrasmall size (~10 nm) by high-temperature alcoholysis esterification, which can be tuned by varying the relative ratio of oleyl alcohol/oleic acid.[53] High-quality Al-doped ZnO NCs synthesized by Milliron et al. show tunable LSPR in NIR region,[51] which were prepared by a rational alcoholysis strategy. Metal chalcogenide NCs can be synthesized mainly through variation of metal-chalcogen ratios.[54-57] For example, Xu et al. synthesized $Cu_{2-x}S$ NCs by a one-pot strategy with Cu_3N NPs as copper precursors. Their size can be controlled by the ratio of Cu/S, which affects subsequent plasmonic resonance absorption. For silicon or metal nitride NCs, which are difficult to synthesize by typical conditions of colloidal synthesis due to their high melting points, nonthermal plasma synthesis is often adopted that can circumvent the prerequisite of accurate reactivity balance between dopant precursors and host. [34,58-60] For instance, Kortshagen et al. demonstrated phosphorus-doped silicon NCs with tunable LSPRs in MIR region were synthesized *via* a nonthermal plasma technique.[58,59]

(2) **Dopant types:** The major dopant types are aliovalent substitutional doping, vacancy doping, and interstitial doping. The definition of aliovalent doping is that the elemental impurities are inserted into the host lattice by an interstitial or substitutional doping mechanism, which can donate a free electron or hole to the conduction or valence band, respectively. Balancing reactivity between host and dopants during NCs growth is requirement of interstitial or substitutional doping in NCs.[21,28,61-63] Hutchison et al. reported the synthesis of In_2O_3 NCs substitutionally doped with Zn, Cu, Co, Fe, and Mn *via* slowly adding metal oleates into hot, long-chain alcohol.[61] Banin et al. found that replacement of In^{3+} in InAs with Ag^+ by substitutional doping enables control of the band gap and Fermi energy.[63] Hard-soft acid-base (HSAB) theory by Pearson and others is of great importance for strategically incorporating dopants into NCs during their growth, where affinity between Lewis bases (organic ligand) and Lewis acids (metal ion) should be considered.[64] In addition, the ionic radius of substitutional dopant ions also has an important implication for lattice strain of NCs. Similar ionic radius between host metals and dopant permits to directly tune the carrier concentration without disruption of the crystallographic phase and then influences plasmonic property. For this trend, an example was offered by comparing the radius of Zn^{2+} (60 pm) with that of trivalent dopants.[65] Compared to other cations, the more efficient lattice substitution should occur on In^{3+} cation because its radius (62 pm) has a better match with that of Zn^{2+} rather than Ga^{3+} (47 pm) and Al^{3+} (39 pm), which leads to a LSPR blue-shift. In vacancy-doped or self-doped NCs, the control of the free charge carrier density depends on the tuning of the stoichiometry (for example, oxygen vacancies (O_V) in Sn-doped In_2O_3, Cu vacancies in $Cu_{2-x}S$). Even without extrinsic dopant ions, vacancies can still introduce either free electrons or free holes. In metal chalcogenide NCs, free holes induced by cation vacancies determine the LSPR characteristics. Frenkel et al. studied the influence of vacancy doping of Cu_2S NCs on the LSPR energy in NIR region, which is induced by copper vacancy and related free holes with the variation of I (iodine)/Cu ratios.[66]

(3) **Activated dopant concentration:** To understand how dopants perturb the host lattice and change free carrier concentration, we must study the material's electronic structure and the defect chemistry of the crystals after discussing the reaction kinetic for achieving dopant incorporation.[67, 68] For instance, Mason et al. reported that the content of Sn in Sn-doped In_2O_3 NCs controls the concentration of O_V and activated Sn_{In} substitutional defects. And the concentration of free carriers and related LSPR response of the NCs depend on the concentrations of activated dopant sites and O_V. In addition, Radovanovic et al. reported that controlling the

competition between doping concentration and electron trapping allowed them to generate LSPR in Ti-doped In_2O_3 NCs synthesized by colloidal method deep in the MIR region, and tuned the absorption spectra from 650 cm^{-1} to 8000 cm^{-1}.[69] Recently, they also demonstrated a robust electron polarization in degenerately doped In_2O_3 NCs, enabled by non-resonant coupling of cyclotron magneto-plasmonic modes with the exciton at Fermi level, which is one of the most interesting and novel results.[70,71] Dopants also impact the scattering of free charge carrier within the NCs as well as determining the free carrier concentration.[48,49,72-76] Granqvist et al. in 1984 demonstrated that ionized impurity scattering is the dominating damping mechanism of the free electrons by the experimental and theoretical calculation. For example, Sn/In_2O_3 NCs have a lower near-field enhancement (NFE) around LSPR-active NCs than that of Ce:In_2O_3 NCs owing to its stronger scattering of the charge carrier. Generally, Ce dopant orbitals hybridize far more weakly than Sn orbitals, which is close to the conduction band (CB) minimum in the In_2O_3 host lattice. Construction of heterostructures or codoping with dopant endows semiconductor NCs multifunctional properties. Heterostructures, typically exhibiting synergistic multilevel coupling effect by integrating different component with diverse properties, have been used as tandem electronic systems in which the functional properties of the metals can be enhanced by excitation in the LSPR-active semiconductor.[48,75-77]. For example, in Au-$Cu_{2-x}S$ core-shell-type hybrid nanocrystals, hot electrons in the efficient interface that are transferred from the plasmonic $Cu_{2-x}S$ NCs to Au can efficiently improve the catalytic activity of Au for photocatalytic reactions.[77,78] Similar case also happens in Pd/$Cu_{2-x}S$ heterostructures where hot electrons induced by LSPR of $Cu_{2-x}S$ NCs promote the photooxidation of benzyl alcohol.[78] In addition, codoping is another promising strategy for effectively tuning the dopant population by introduction of multifunctionality, such as plasmonic property together with magnetic property. For example, Mn-Sn codoped In_2O_3 NCs synthesized by Nag et al. enhance magnetization as well as shifts the LSPR band toward longer wavelengths.[79-82] Such enhanced property of NCs also appears in Fe, Sn-codoped In_2O_3 NCs. Considering the semiconducting nature of the host material, postsynthetic method is a useful dynamic knob to modulate LSPR characteristic by tuning carrier concentration.[83] Postsynthetic tuning can be performed according to three main approaches: chemical redox reactions, photochemical charging, and electrochemical charging and discharging.[84-94] $Cu_{2-x}Se$ and $Cu_{2-x}Te$ NCs have demonstrated that oxidation/reduction of reducing/oxidizing agents is a typical way to realize the reversibility of postsynthetic tuning of the LSPRs, which involves electron transfer from or to NCs.[83] Photochemical charging allows protons to add the NCs in a stoichiometric fashion, which can stabilize free electrons of conduction band by a hole scavenger.[84-86] For example, Mayer et al. found that the redox chemistry of dodecylamine-capped ZnO NCs is strongly influenced by the addition of few protons in toluene/THF solutions.[86] Electrochemical charging or discharging of the samples in the form of films has an important impact on the concentration of valence band (VB) holes or conduction band (CB) electrons. Postsynthetic electrochemical modulation of the electron concentration can dynamically and reversibly tune LSPR of Sn-doped In_2O_3 NCs film, which induces a shift (> 1200 nm) in the plasmon wavelength. Based on the potential of NFE characteristics and scattering in addition to resonant absorption, applications of plasmonic semiconductor NCs have been explored in many fields, e.g., the photothermal effect of plasmonic NCs, which refers to heat generated by absorption of light, has been introduced for biomedical therapy, imaging and so on. The possibility to tune the LSPR of NCs in NIR has been applied for IR enhancing spectroscopies.

In this review, we will focus on the three widely explored and interrelated examples including (1) hydrogen molybdenum bronzes (H_xMoO_{3-y}) NCs, (2) hydrogen tungsten bronzes (H_xWO_{3-y}) NCs, and (3) oxygen vacancy doped molybdenum tungsten oxide ($Mo_xW_{1-x}O_{3-y}$) NCs. Each section contains the introduction of their own hybrids. In previous reviews, owing to generally very similar properties of the first two types of NCs, they are simply discussed together. Instead, here we designed to provide a separate description of the important plasmonic property in NCs and their manipulation methods of LSPR. Finally, we will give a brief outlook toward applications of these plasmonic NCs.

2. Fundamental Properties

2.1 Stoichiometric MoO_3

Two crystal phases of MoO_3 are commonly found: the thermodynamically stable orthorhombic α-phase and the metastable monoclinic β-phase, which are constructed in different ways based on MoO_6 octahedron units (**Fig. 1a**).[95-98] Orthorhombic α-MoO_3 possesses a unique layered structure along the *b* axis (**Fig. 1b**), which offers the possibility of forming a two-dimensional (2D) morphology.[96,99-104] The dual layer planar crystals in α-MoO_3, which are formed by atomically thin sheets featuring a thickness of ≈ 1.4 nm, consist of MoO_6 octahedra by corner-sharing rows and edge-sharing zigzag rows along the [100] and [001] directions, respectively.[95] The interactions between atoms of the distorted MoO_6 octahedra are dominated by strong ionic bonds and covalent bonds, while the octahedra are stacked up in the vertical [010] direction by relatively weak van der Waals forces. Owing to different coordination, three types of oxygen atoms exist in the crystal structures (**Fig. 2**) (i.e., symmetrically bridging (O_s), asymmetric (O_a), terminal (O_t)). The O_s bonds to three Mo atoms with one vertical bond and two horizontal bonds and the bond lengths are 2.33 and 1.95 Å, respectively. The O_a bonds with two Mo atoms with length of 2.25 and 1.74 Å, respectively. The O_t bonds to only one Mo atom and the mean length is 1.67 Å. Unlike α-MoO_3, β-MoO_3 adopts a monoclinic 3D structure, where the MoO_6 octahedra cannot crystalize in double layers and cannot share in zigzag rows along the [001] plane (**Fig. 1c**). And the 3D structure that originates from the corner-sharing of the MoO_6 octahedra is not desirable for forming planar crystals.[105-108] In addition, it has been reported that β-MoO_3 phase is generally transformed into the α-MoO_3 on account of thermal treatments at above 350 °C. For some specific applications, some studies demonstrate that *β*-MoO_3 generally has better catalytic properties than *α*-MoO_3.[101,109] However, such properties are generally attributed to the grain size effects rather than the result of the crystal phases when samples have similar grain morphologies and dimensions. Another two less known metasftable polymorphs oxides also exist hexagonal *ε*-MoO_3 and *h*-MoO_3 (**Fig. 1d-f**).

2.2 Non-stoichiometric MoO_3

As an n-type semiconductor material, MoO_3 has many significant applications in catalysis, gas sensors, and optoelectronics. However, the bandgap of ca. 3.2 eV means that MoO_3 can only adsorb energy from the UV light spectrum, which occupies less than 5% of the solar energy. Considering its unique layered structure, molybdenum bronze ($A_xMo_yO_z$) as a fantastic

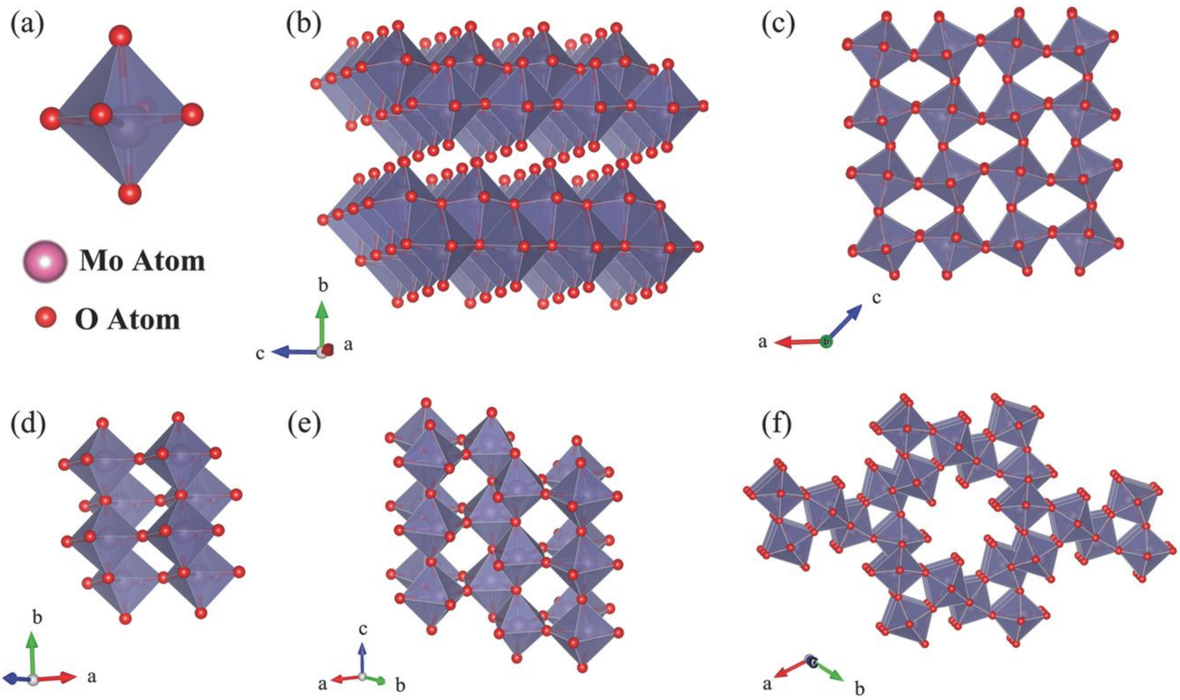

Fig. 1. a) MoO_6 octahedra as found in the thermodynamically stable *α*-MoO_3 composed of molybdenum and oxygen atoms. b) Thermodynamically stable orthorhombic *α*-MoO_3 with layered structure held together by van der Waals' forces. c) Metastable monoclinic *β*-MoO_3. d) *ε*-MoO_3, also known as MoO_3-II. e) Metastable *h*-MoO_3. f) Tunnel structure along the *c*-axis of *h*-MoO_3 unit cell. Reproduced with permission from Ref. [103]. Copyright 2017 Wiley-VCH.

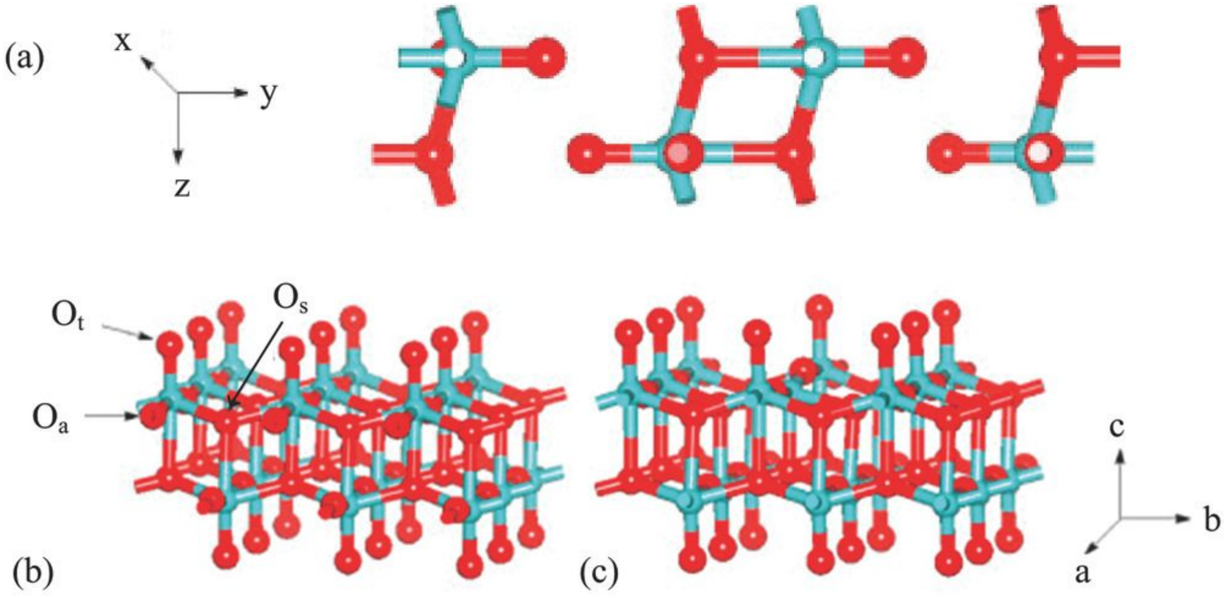

Fig. 2. a-c) Crystal structures of *α*-MoO_3 bulk form (a), and perfect (b) and terminal defect (010) (c) surfaces. Reproduced with permission from Ref. [103]. Copyright 2017 Wiley-VCH.

compound can be developed by intercalating cations into the van der Waals gap and accompanied by the partial reduction of Mo oxidation states, where A may be an alkali metal cation (such as Li^+, Na^+, K^+), hydrogen, and Tl^+.[110,111] These bronzes structures drive their metallic character partially occupied 4d-bands while MoO_3 is an insulator with an unfilled 4d band. Since hydrogen bronzes H_xMoO_{3-y} were obtained in 1950 by Glemser and Lutz by ambient-temperature reactions,[112] H_xMoO_{3-y} has been researched widely. The intercalated H^+ cations primarily bind to terminal oxygen atoms and edge-shared oxygen leading to the formation of intermediate OH_2 groups in the H_xMoO_{3-y} structure.[113,114] A more complete and specific research by Dickens and Birtill showed that H_xMoO_{3-y} has four distinct phases: stoichiometric phase I (H_2MoO_3, green colour), phase II ($H_{1.55-1.72}MoO_3$, red, monoclinic), phase III ($H_{0.85-1.04}MoO_3$, blue, monoclinic), and phase IV ($H_{0.23-0.40}MoO_3$, blue, orthorhombic)[99,115] The properties of H_xMoO_{3-y} change dramatically with the variation of hydrogen content while the crystal structure of their parent MoO_3 generally remains constant.[99] The semiconductor-metal transition happens at specific temperature, which was demonstrated by the electric conductivity measurements on H_xMoO_{3-y} powder.[116] Many previous important work has been concentrated on the understanding of how to construct free carriers and the semiconductor to metal transition process induced by free carrier gas or Fermi surface nesting.[117,118]

2.2.1 Synthesis and Applications of H_xMoO_{3-y} NCs.

Reasonable design of the synthesis route of H_xMoO_{3-y} can realize the modification of free carriers concentration and afterwards control plasmon tuning over a wide spectral range, which makes this material very appealing for numerous applications. In 1988, Greenblatt et al. reported a series of solid phases H_xMoO_{3-y} by electrochemical or chemical reduction of MoO_3 in acidic media, which was first put forward by Glemser et al. and consummated by Dickens and Birtill in 1979.[119] Similar synthesis methods were also adopted by many later researchers.[115-117] At ambient temperature, electrochemical reduction in aqueous acidic media ($MoO_3 + xH^+ + xe^- \rightarrow H_xMoO_3$) or chemical reduction using H^+/metal couples (e.g., HCl/Zn) results in the formation of hydrogen molybdenum bronzes.[118] By comparing their lattice parameters with those of MoO_3 (**Table 1**),[118] minimal structure rearrangement occurs when hydrogen is inserted into the MoO_3 matrix.

Table 1. Unit cell dimensions of H_xMoO_{3-y} bronze phases. Reproduced with permission from Ref. [118]. Copyright 1988 American Chemical Society.

H_xMoO_{3-y}	color	*a*, Å	*b*, Å	*c*, Å	*β*, deg	space group
$H_{0.34}MoO_3$	blue	3.8	14.0	3.7	90.0	orthorhombic
$H_{0.93}MoO_3$	blue	14.5	3.7	3.8	93.7	monoclinic
$H_{1.68}MoO_3$	red	13.9	3.7	4.0	93.9	monoclinic
$H_{2.0}MoO_3$	green	13.5	3.8	4.0	94.6	monoclinic
MoO_3[a]		3.9	13.8	3.6	90.0	orthorhombic

[a] *a,b,c* orthorhombic → *b,a,c* monoclinic

The presence of OH and OH_2 groups are evidenced by the inelastic neutron scattering spectra of H_xMoO_{3-y}, in which H atoms bond to the bridging oxygen atoms (O_s) and the terminal oxygen atoms (O_t), respectively. Afterwards, hydrothermal and solvothermal syntheses of plasmonic H_xMoO_{3-y} NCs have been immensely developed by subsequently ameliorated nonhydrolytic colloidal synthesis.[105,120] For example, Hu et al. reported a hydrothermal method to synthesize MoO_3 nanobelts from Mo powders and H_2O_2 solution, which can be reduced to H_xMoO_{3-y} nanobelts by using the reducing agent ($N_2H_4{\cdot}H_2O$) under an acidic condition. Hydrogen doping greatly improves the conductance of H_xMoO_{3-y} nanobelts. The exponential correlation between temperature and resistances of H_xMoO_{3-y} nanobelts supports that the quasi-free electrons released from Mo^{5+} are the conducting carriers.[115]

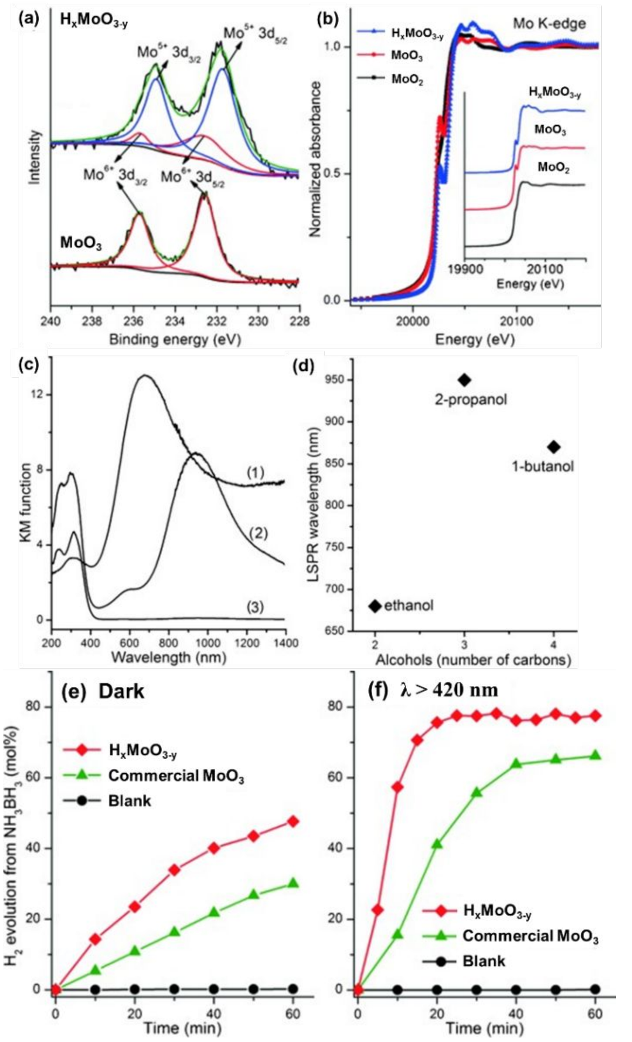

Fig. 3. a) Mo 3d XPS spectra of the as-prepared H_xMoO_{3-y} and commercial MoO_3 samples. b) Mo *K*-edge XANES spectra of H_xMoO_{3-y} and reference materials (commercial MoO_3 and MoO_2). c) UV/Vis-NIR diffuse reflectance spectra of the H_xMoO_{3-y} samples prepared at 160 °C (1) and 140 °C (2) for 12 h, and commercial MoO_3 (3). d) The LSPR wavelength of the products prepared by different alcohols in the solvothermal synthesis. Time course of H_2 evolution from NH_3BH_3 aqueous solution at room temperature for different samples: e) in the dark and f) under visible light irradiation (λ > 420 nm). Reproduced with permission from Ref. [98]. Copyright 2014 Wiley-VCH.

H_xMoO_{3-y}-oleylamine composite with ultrathin blue nanosheets is successfully synthesized by Huang et al. by hydrothermal treatment at 180 °C, where a water/oil emulsion is prepared by mixing cyclohexane, water and oleylamine together. The presence of a certain amount of oleylamine and oxidant drives the blue nanosheets to curve into white nanotubes. Electron spin resonance (ESR) and the X-ray photoelectron spectroscopy (XPS) results confirm that the color change is attributed to the oxidation of Mo^{V} to Mo^{VI}, which is induced by the variation of Ov.[105] In this process, tunable LSPR is obviously observed as the oxidation reaction undergoes gradually. The initial blue nanosheets prominently present the photothermal effect under the irradiation of an NIR laser owing to the strong LSPRs. In the past five years, many research groups have made outstanding achievements in this field, among which prof. Yamashita's team is a pioneer. They reported that well-defined H_xMoO_{3-y} nanosheets were prepared by solvothermal method (non-aqueous procedure) in the absence of surfactants, where the solution-soluble precursor compound $MoO_2(OH)(OOH)$ was prepared by using H_2O_2 to dissolve pure Mo powder in the ethanol solution. During the synthesis process, ethanol plays two important roles: (1) it supplies a mild condition for abating the violent reaction between H_2O_2 and Mo powder, and (2) it acts as a reductant to reduce MoO_3 into blue H_xMoO_{3-y} at higher solvothermal temperatures. XPS spectra and Mo *K*-edge XANES spectra all demonstrate that valence of Mo species in H_xMoO_{3-y} is located between MoO_3 and MoO_2 (**Fig. 3a-b**). The obtained H_xMoO_{3-y} nanosheets show strong plasmonic absorption peak in a wide range (**Fig. 3c**), which is tuned from the visible to the NIR by using different alcohol in the solvothermal synthesis (**Fig. 3d**). Such plasmonic H_xMoO_{3-y} NCs can dramatically enhance the dehydrogenation performance of ammonia borane under visible light irradiation relative to dark condition (**Fig. 3e-f**).[98,102] However, the preferential formation of 2D MoO_3 nanosheets will be available due to the intrinsic anisotropic crystal growth, which usually leads to very small surface area, accompanied by relatively low catalytic activity. Given that this point, during liquid-based synthesis processes, surfactant orientating and templating can be used for shaping MoO_3. For example, relative high-surface-area and well-crystallized MoO_3 was hence prepared by evaporation induced self-assembly (EISA) process. Subsequently, plasmonic H_xMoO_{3-y} NCs were synthesized by hydrogen reduction method via a postsynthetic process. In this synthetic process, F127 as a surfactant efficiently inhibits the intrinsic growth process of tiny MoO_3 nuclei to MoO_3 nanosheets, which causes much smaller nanosheet size and then increases specific surface area. The prepared H_xMoO_{3-y} with high surface area shows temperature-dependent LSPR in the visible region, which supports a relatively high NH_3BH_3 dehydrogenation activity. Suib et al. developed a more effective approach to synthesize mesoporous H_xMoO_{3-y} with nanosized crystalline walls.[108] In the synthesis process, tetrahydrofuran (THF) as a solvent instead of ethanol is chosen to dissolve a soft template (PEO-*b*-PS) without self-assembly aggregation, which is key to form mesoporous structure in subsequent aging.[102] For electrochemical hydrogen evolution reaction (HER), the as-synthesized mesoporous H_xMoO_{3-y} NCs show very stable (durability > 12 h) and active performance under alkaline and acidic conditions (**Scheme 1**). Postsynthetic control provides a dynamic adjustment of LSPR characteristics in semiconductor NCs that far surpasses what is possible with metal NPs, which contains several methods such as electrochemical reactions, photochemical, or oxidation/reduction. Postsynthetic control for tuning LSPR peak of H_xMoO_{3-y} was further verified by Li et al. by using different reductants.[102] For example, highly stable MoO_3 nanodots have been designed and prepared by the oxidation of bulk MoS_2 ($MoS_2 + 9H_2O_2 \rightarrow MoO_3 + 7H_2O + 2H_2SO_4$). Subsequently, substoichiometric H_xMoO_{3-y} nanodots are obtained from MoO_3 with different reducing agents, including ascorbic acid (AA) and $NaBH_4$. Although $NaBH_4$ leads to a different substoichiometric oxide and XPS analysis shows substantial increase of valence state of Mo (V), it cannot have LSPR peak tunability when reaction finishes. By controlling the reducing concentration, the weaker reductant AA successfully realizes a dynamic tunability of plasmonic energy resonance, which can modulate LSPR features at around 700 - 1000 nm.

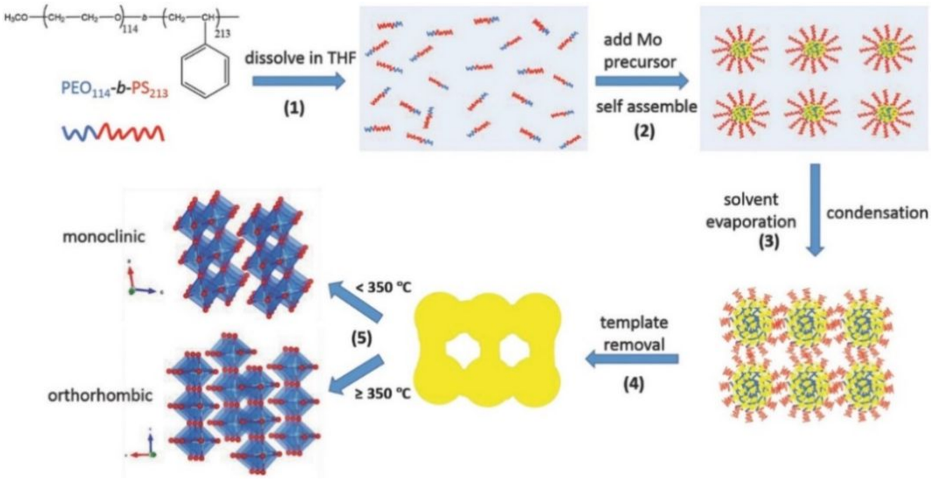

Scheme 1. The proposed formation mechanism of inverse micelle-templated mesoporous H_xMoO_{3-y}. Reproduced with permission from Ref. [108]. Copyright 2016 Wiley-VCH.

From the above results, it indicates that the right choice of reducing agents in postsynthetic process plays a crucial role in controlling plasmon tuning over a wide spectra range. Zhang et al. synthesized plasmonic H_xMoO_{3-y} nanosheets by solvothermal procedure with methanol as a solvent and as a reducing agent. Core-shell structured H_xMoO_{3-y}@MoO_3 nanosheets with various LSPR frequencies and intensities were obtained after the calcination process. Such plasmonic NCs with preserved free carrier concentration show extraordinary sensitivity on surface-enhanced Raman scattering (SERS) detection, which is ascribed to the shell-isolated electromagnetic enhancement by H_xMoO_{3-y} core.[121] Of course, the synthetic methods of plasmonic H_xMoO_{3-y} are not only limited to hydrothermal and solvothermal method or templating and surfactant methods, but also can be extended to other routes, such as exfoliation method, H_2 plasma etching. For example, Kalantar-zadeh et al. successfully synthesized yellow/blue H_xMoO_{3-y} nanosheets with oxygen deficiency by a liquid phase exfoliation method, where high power untrasonication was used to grind bulk MoO_3 with ethanol, facilitating mechanical liquid phase exfoliation. The as-synthesized 2D H_xMoO_{3-y} shows a considerable electrocatalytic HER performance with a fast electron transfer and low overpotential. Mai et al. also reported that oxygen-deficient α-H_xMoO_{3-y} was synthesized by H_2 plasma etching, which could reduce bandgap and expand van der Waals gap. Electrochemical test results indicate H_xMoO_{3-y} has high Li^+ diffusion coefficient, the slight polarization and low charge transfer resistance.[122] In conclusion, a variety of methods have been used for synthesizing substoichiometric H_xMoO_{3-y} NCs both in liquid- and gas-phase media. Such plasmonic H_xMoO_{3-y} NCs have also found more and more applications in many fields, such as photocatalysis, electrocatalysis, photothermal therapy and so on.

2.2.2 Synthesis and Applications of H_xMoO_{3-y} Hybrids

Single-component materials are normally confined by their intrinsic properties in heterogeneous catalysis, such as weak light absorption and low catalytic efficiency, and consequently they are unable to fulfill the functional demands. On the contrary, hybrid materials have received more and more attention, because they show synergistic multilevel coupling effect owing to different components with diverse properties.[123] Hence, despite the challenges, it is important and intriguing to develop efficient synthetic methods to prepare plasmonic H_xMoO_{3-y}-based hybrids, which could further improve optical properties and catalytic performances. For example, deposition of active metal catalysts (e.g., Pd) on plasmonic H_xMoO_{3-y} can have more extensive catalysis reaction opportunities, such as Suzuki coupling reactions and *p*-nitrophenol reduction. Yamashita et al. developed a solution-processed impregnation-reduction method to plasmonic Pd/H_xMoO_{3-y} hybrid by coupling metal NPs and H_xMoO_{3-y} NCs, which is extended to Au/H_xMoO_{3-y} and Pt/H_xMoO_{3-y} hybrids as well.[124] The Pd/H_xMoO_{3-y} hybrid was synthesized by introducing reductant $NaBH_4$ into the suspension of $PdCl_4^{2-}$ ions and MoO_3 support, which were reduced to Pd^0 NPs and H_xMoO_{3-y} simultaneously (**Fig. 4a**). Such a Pd/H_xMoO_{3-y} hybrid shows strong LSPR absorption peak under visible light range, displaying dramatic plasmon-improved catalysis in Suzuki-Miyaura coupling and dehydrogenation of NH_3BH_3 under visible light irradiation.[124] One interesting property of the Pd/H_xMoO_{3-y} hybrid is that their LSPRs exhibit reversible tunability upon reduction by $NaBH_4$ in solution and oxidation by O_2 under air (**Fig. 4b**). During the gradual oxidation by O_2 in air, phase structures of Pd/H_xMoO_{3-y} hybrid are found no obvious changes, the plasmonic absorption peaks, however, change from a symmetrical narrow band to an asymmetrical broader, then shift to a broader band in NIR region and eventually disappear. Through reduction by $NaBH_4$ in solution, the LSPRs of the oxidized Pd/H_xMoO_{3-y} hybrid can be restored (**Fig. 4c**), which still shows an intense plasmonic resonance, approaching the original one. In addition, Cheng et al. found that the presence of a metal such as Pd drives MoO_3 to reduce at lower temperature.

Through H_2 reduction process, massive activated H atoms are inserted into the layered structure of orthorhombic MoO_3 host, resulting in the distortion of MoO_6 octahedra (**Fig. 5a**), where H atoms bond strongly with terminal oxygen atoms. Before H_2 reduction, only a small absorption peak in UV region (shorter than 400 nm) is found in Pd/MoO_3 hybrid. On the contrary, Pd/H_xMoO_{3-y} hybrid shows strong absorption peak in the visible light range (**Fig. 5b**). Prior to H_2 reduction, Mo species of Pd/MoO_3 hybrid only contain Mo^{6+} ions as shown in the XPS spectra of Mo 3d core level (**Fig. 5c**). However, not only Mo^{6+} but also Mo^{5+} and Mo^{4+} ions exist in the Pd/H_xMoO_{3-y} after H_2 reduction at RT. First-principles DFT calculations are also used to study the electronic structure of the hydrogen bronzes. The projected density of states (PDOS) and total density of states (TDOS) of pristine MoO_3 are presented in **Fig. 5d,e**. Apparently, no vacancies states are present in pristine MoO_3 with the bandgap of around 1.9 eV. In contrast, H_xMoO_{3-y} hybrid shows strong metallic feature with continuous VB across the Fermi level into the CB (**Fig. 5e**). The intercalation of hydrogen atoms into the MoO_3 matrix results in the drastic changes in electronic structures of H_xMoO_{3-y} hybrid.

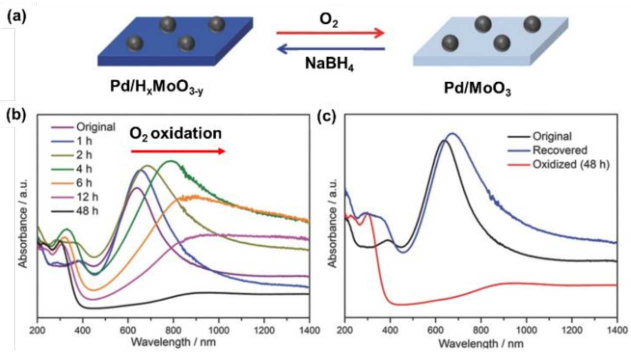

Fig. 4. a) Schematic illustration of the Pd/H_xMoO_{3-y} hybrid upon oxidation by O_2 in air and reduction by $NaBH_4$ in solution. b) The evolution of the optical response of Pd/H_xMoO_{3-y} hybrid exposed to air for different time periods. c) The optical absorption for the original Pd/H_xMoO_{3-y} hybrid, oxidized in air for 48 h, and the recovered product by $NaBH_4$ reduction. Reproduced with permission from Ref. [124]. Copyright 2015 Wiley-VCH.

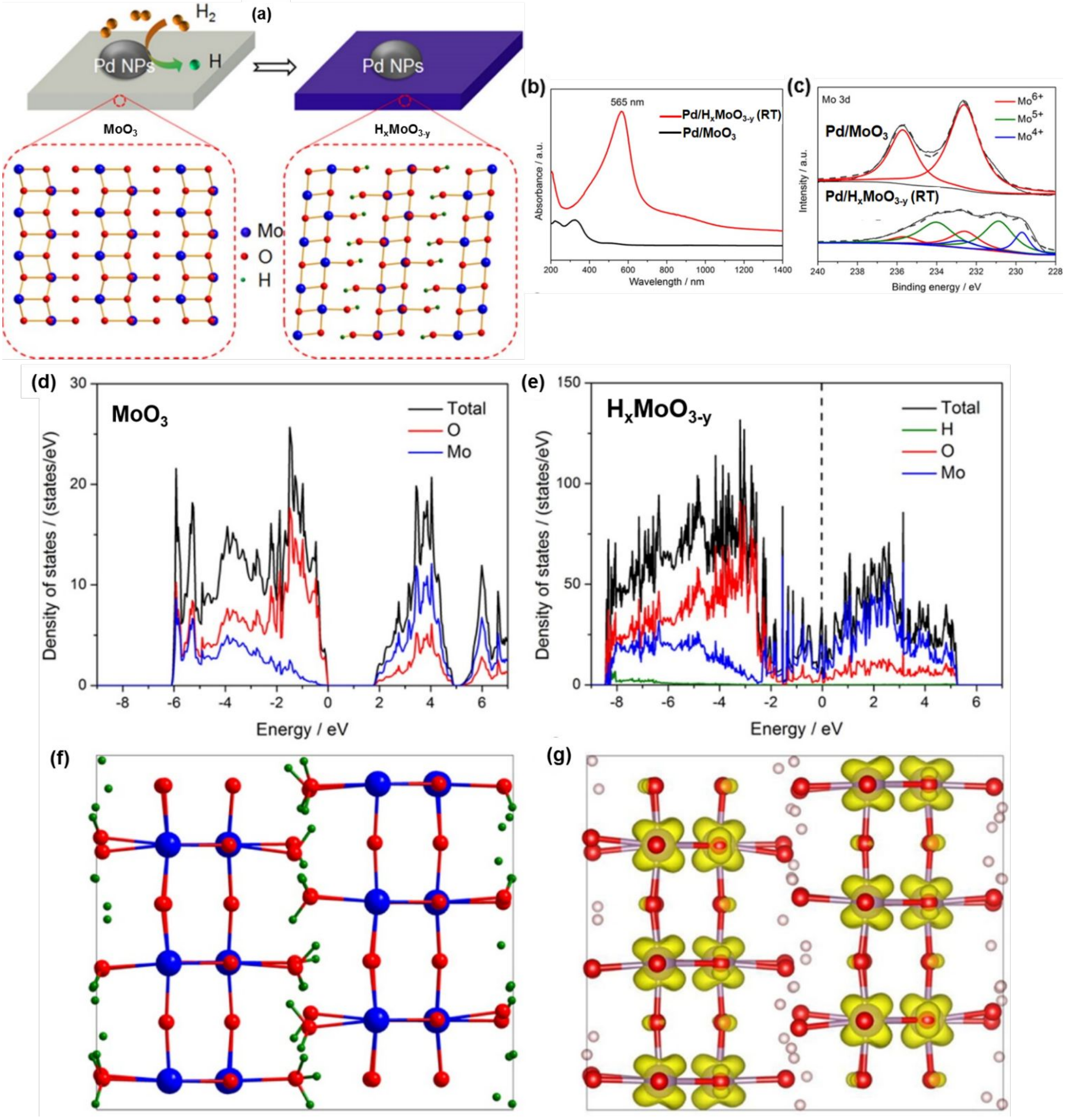

Fig. 5. a) Schematic diagram of the formation of hydrogen bronzes *via* H-spillover process. Optical and structural characterizations of hydrogen molybdenum bronze. b) UV-vis–NIR diffuse reflectance spectra and c) Mo 3d XPS spectra of Pd/MoO_3 products before and after H_2 reduction at room temperature. Density functional theory calculations. TDOS and PDOS of d) pure MoO_3 and e) heavily hydrogen-doped H_xMoO_{3-y}. f) Structure illustration for H_xMoO_{3-y} in (010) projection. Blue balls represent Mo atoms, red for O, and green for H atoms. g) Three-dimensional visualization of electronic charge density distribution around the Fermi level for H_xMoO_{3-y}. Reproduced with permission from Ref. [125]. Copyright 2016 American Chemical Society.

Massive H atoms are inserted into the interlayer positions of the layered structure of orthorhombic MoO_3 (**Fig. 5f**), which results in the distortion of MoO_6 octahedra. Subsequently, the electrons of activated hydrogen 1s orbital transfer to the O 2p orbital and further shift to the coordinating Mo atoms, leading to a partial reduction of Mo^{6+}. Furthermore, the introduced electronic charge is uniformly distributed on Mo atoms due to the delocalization nature of Mo 4d electrons, which is proved by the 3D visualization of electronic charge density distribution for H_xMoO_{3-y} (**Fig. 5g**). The logical explanation is that a partially filled π^* is generated by the intermediary O $2p_\pi$ orbitals with Mo 4d orbitals of t_{2g} symmetry overlap, which shifts their Fermi level within the CB. Therefore, with such high degree of delocalization in the visible light spectrum, free electrons donated by hydrogen atoms are expected to support the LSPRs. Under visible light irradiation, these electrons of plasmonic H_xMoO_{3-y} support will quickly transfer to the adjacent Pd NPs. That is, H_xMoO_{3-y} supports are positively charged and the surface of Pd NPs is negatively charged, which hence enhances the catalytic performance of dehydrogenation of NH_3BH_3 and the reduction activity of *p*-nitrophenol.[124,125] As we all know, for the chemoselective hydrogenation of unsaturated aldehydes to saturated aldehydes, Pd-based catalysts play a key role. It, however, is still difficult to get high selectivity and conversion. A lot of progress have been made by modulating electron density of catalytic sites on Pd-based catalysts.[125] Imran et al. integrated the advantages of 2D H_xMoO_{3-y} nanosheets and active monodispersed Pd nanotetrahedrons to synthesize hybrid nanocatalyst with high performance to convert α,β-unsaturated aldehydes to the corresponding saturated aldehydes. The as-synthesized Pd/H_xMoO_{3-y} hybrid is synthesized *via* a simple one-pot wet-chemical synthetic method, where DMF and toluene act as solvents and PVP and CTAB are used to control the morphology of Pd NCs.[123] Kuwahara et al. proved for the first time that plasmonic Pt/H_xMoO_{3-y} hybrid exhibits a higher catalytic activity under visible light irradiation relative to dark conditions in the reaction of the deoxygenation of diphenyl sulfoxide (DPSO). The preparation of plasmonic Pt/H_xMoO_{3-y} hybrid is obtained *via* a facial H-spillover process (**Fig. 6a**). At controlled temperature (RT, 100 °C, and 200 °C), Pt ions and α-MoO_3 are reduced simultaneously in a flow of H_2. By *in situ* formed Pt NPs in the above process, a rapid dissociation of H_2 is occurred ($H_2 \rightarrow 2H^+ + 2e^-$) and subsequent free electrons and H^+ are injected into MoO_3 matrices, where the reduction temperature can easily modulate the vacancies densities and the H+ dopant levels. As shown in **Fig. 6b**, Pt/H_xMoO_{3-y} hybrid shows a strong LSPRs absorption peak around 556 nm compared with Pt/MoO_3 hybrid without H_2 reduction. With the reduction temperature raises, the increased concentration of free carriers not only leads to an intensification of the absorption peaks but also results in a blue shift of the plasmonic wavelength.

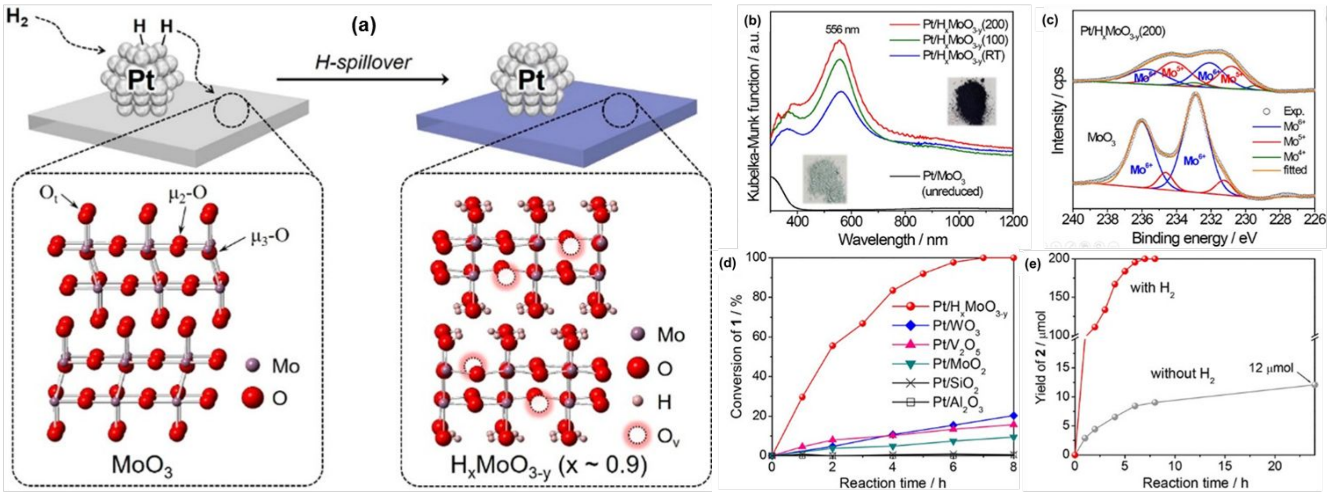

Fig. 6. a) Schematic illustration of the formation of hydrogen molybdenum bronzes (H_xMoO_{3-y}) *via* a H-spillover process. b) UV–vis-NIR diffuse reflectance spectra for the Pt/H_xMoO_{3-y} hybrids reduced at varied temperatures and for the unreduced Pt/MoO_3. c) Mo 3d XPS spectra for the Pt/H_xMoO_{3-y} (200) and pristine MoO_3. Time course in the deoxygenation of diphenyl sulfoxide over d) various Pt-loaded oxide catalysts (reduction temperature = 200 °C). e) Time course of the yield of diphenyl sulfide over Pt/H_xMoO_{3-y} (200) catalyst with or without H_2. Reproduced with permission from Ref. [126]. Copyright 2018 American Chemical Society.

In Mo 3d XPS spectra (**Fig. 6c**), Mo species of Pt/H_xMoO_{3-y} (200) hybrid are mainly occupied by Mo^{6+} species in addition to lower oxidation states. In the deoxygenation of diphenyl sulfoxide (DPSO), plasmonic Pt/H_xMoO_{3-y} hybrid shows the highest catalytic performance in 7h of reaction with > 99% yield (**Fig. 6d**). Pt/Al_2O_3 and Pt/SiO_2 do not exhibit any catalytic activities, which indicates that the main active sites in this reaction are not Pt NPs. Furthermore, plasmonic Pt/H_xMoO_{3-y} hybrid still has a certain yield even in the absence of H_2, verifying the Ov sites are the main active sites for deoxygenation reaction (**Fig. 6e**). Comprehensive analyses by means of XPS, ESR, and Raman spectroscopy indicate that the strong LSPRs and massive Ov provide an effective catalytic system for the deoxygenation of DPSO.[126] Recently, an important and intriguing phenomenon has been found by Yamashita et al. that activated hydrogen species of H_xMoO_{3-y} hybrid show excellent mobility on certain metals (e.g., Ru). Ru/hydrogen molybdenum bronzes (Ru/H_xMoO_{3-y}) are prepared *via* a facial H-spillover route. Detailed characterization reveals that Ru/H_xMoO_{3-y} exhibits strong visible light absorption with a plasmonic peak (**Fig. 7a**), which is tunable by varying the reduction temperature of H_2 gas. Under visible light irradiation relative to dark condition, Ru/H_xMoO_{3-y} hybrid displays superior catalytic activity in the photocatalytic reduction of *p*-nitrophenol (**Fig. 7b**), where Ru NPs act as the active centres and H_xMoO_{3-y} support serves as electron-donation centres. Furthermore, both hydrogen species in H_xMoO_{3-y} originating from H-spillover process and the excited electrons transfer to Ru NPs surface under visible light irradiation, thereby leading to the reduction of the $-NO_2$ group to the $-NH_2$ group, which is fully demonstrated by catalytic activity (**Fig. 7c**).[127] The mobility exploration of activated hydrogen species in H_xMoO_{3-y} is an interesting and valuable research. Precious metals as the commonly co-catalyst with large work function are used to capture the photoexcited carriers and drive the reduction reaction of protons. Nevertheless, the scarcity and high cost of noble metals cannot realize the practical application, and thus developing earth-abundant, efficient, and stable co-catalyst is still a formidable challenge in many fields. Peng et al. reported that Mo-based cocatalyst (MoS_2-α-MoO_{3-x} with oxygen-deficient) is grafted on the surface of $AgIn_5S_8$ nanooctahedrons *via* an *in situ* growth process, which creates more active sites and then shows an effective enhancement of visible-light-driven H_2 evolution. α-MoO_{3-x} NCs with mixed Mo^{5+}/Mo^{6+} oxidation states by partial reduction play a central role in the reaction of H_2 evolution, which enables facial charge transport owing to its high conductivity and oxygen-deficient structure. Seo et al. demonstrated that graphene (mRGO)-MoO_{3-x} nanohybrid shows a superior reversible and flexible electrochromic (EC) application.[128] The synthesis of this nanohybrid was performed by equipment-free Langmuir-Blodgett (LB) film deposition method, in which mRGO-MoO_{3-x} hybrid has a strong possibility to have a super dispersibility in a water-miscible solvent. Subsequently, even without a need for a trough, the self-assembly of the nanohybrid sheets into Langmuir film could also be achieved. Electrons transfer among individual mRGO-MoO_{3-x} sheets is attributed to the good contract among the hybrid sheets, which leads to an excellent EC property with a high coloration efficiency. The requirements of high stability, catalytic activity, and solar photon-to-current conversion cannot be satisfied only by the development of a single material. Meeting the various requirements by utilizing multiple materials is a new strategy. In order to address conductivity limitation in MoS_2 with a high aspect ratio structure, Jaramillo et al. prepared vertically oriented core-shell nanowires (NWs) with MoS_2 shells and H_xMoO_{3-y} cores, where MoO_3 NWs were obtained by a simple hot-wire chemical vapor deposition method and MoS_2 shell layer was synthesized by sulfidized of the supported MoO_3 NWs in a quartz tube furnace under a mixture of H_2S/H_2 gas.[129] The H_xMoO_{3-y} core supplies facile charge transport due to a high aspect ratio foundation, while the MoS_2 shell supplies excellent electrocatalytic hydrogen evolution and stability in strong acids. There are no doubts that such studies will display many promising applications with plasmonic hybrids in solar-energy harvesting, catalysis, magneto-optics, and optoelectronics.

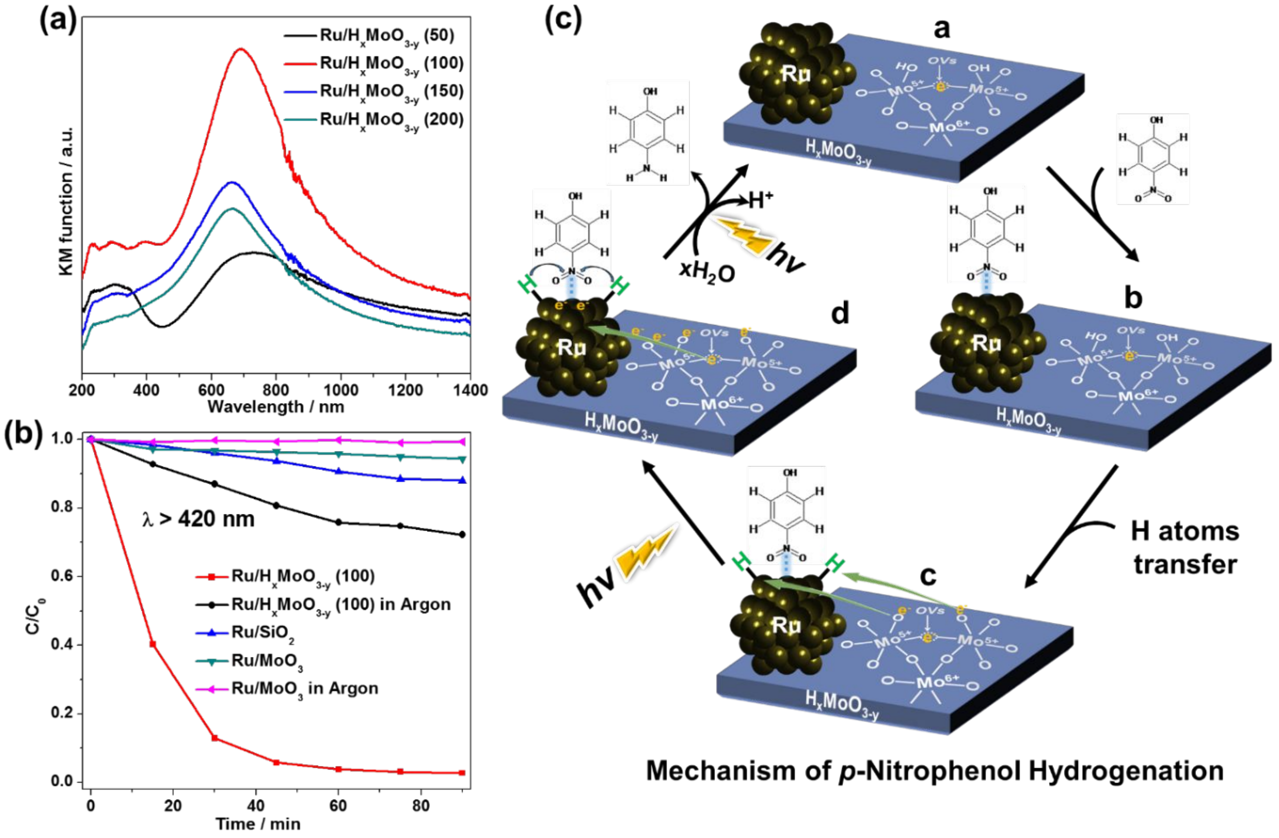

Fig. 7. a) UV-vis-NIR diffuse reflectance spectra of the Ru/MoO_3 samples upon H_2 reduction at different temperatures. b) Plots of relative concentration of *p*-nitrophenol over Ru/H_xMoO_{3-y} (100) catalyst and reference samples as a function of time. c) Proposed mechanism of *p*-nitrophenol hydrogenation on Ru/H_xMoO_{3-y} (100) without H_2 gas atmosphere. Reproduced with permission from Ref. [127]. Copyright 2019 Royal Society of Chemistry.

2.3 Stoichiometric WO_3

WO_3 are also constituted by edge- and corner-sharing of WO_6 octahedra (**Fig. 8**).[130] There are six phases by corner-sharing: tetragonal (α-WO_3), orthorhombic (β-WO_3), monoclinic I (γ-WO_3), triclinic (δ-WO_3), monoclinic II (ε-WO_3), and cubic WO_3. However, cubic WO_3 is not commonly observed experimentally. Similarly, WO_3 crystal phase transitions can occur during cooling and annealing. Phase transformation takes place in bulk form by following sequences: monoclinic II (ε-WO_3, -43 °C) → triclinic (δ-WO_3, -43 °C to 17 °C) → monoclinic I (γ-WO_3, 17 °C to 330 °C) → orthorhombic (β-WO_3, 330 °C to 740 °C) → tetragonal (α-WO_3, > 740 °C). Partially reversible of the above phase transitions of WO_3 has been reported. At subzero temperatures, the monoclinic II phase is only stable. Monoclinic I (γ-WO_3) is the most stable phase at room temperature, where triclinic is also stable. WO_3 will transform to α-WO_3 and β-WO_3 at high temperature, whereas these alternate phases cannot retain when it is returned to room temperature.

2.4 Non-stoichiometric WO_3

Bulk WO_3 (an n-type semiconductor) has a band gap around 2.7 eV and is stable under a wide range of conditions. WO_3 NCs are a particularly interesting system for the research of LSPR in NPs. Tungsten oxide bronzes (TOBs) are solid electrolytes with mixed (cation-electron) conductivity.[131-134] In these substances, a stable sub-lattice is formed by the octahedrons of WO_6, while cations of alkali metals (or hydrogen) are displaced into the empty spaces between octahedrons. These spaces form channels, along which the cations can move. This can withstand a considerable amount of shallow deficiency in the oxide band structure. Creation of one-dimensional channels from WO_6 octahedra in the crystal structure of WO_3 is ideal to incorporate cations owning specific ionic radii, such as Cs^+, Ce^+, Rb^+, and Na^+.[135-137] The chemist Friedrich Wöhler in 1823 prepared sodium tungsten bronze (Na_xWO_3), which was the first alkali metal bronze to be discovered [136]. They owe some of their properties to the relative stability of the tungsten (V) cation that is formed, leading to accumulation of delocalized free electrons in the conduction band. Hydrogen tungsten bronzes are nonstoichiometric materials with the formula of H_xWO_{3-y}, where hydrogen atoms are incorporated into the structure of WO_3. Glemser and Naumann for the first time in 1951 reported that H_xWO_{3-y} was obtained by reduction of tungsten trioxide or tungstates.[138] Dickens and Hurditch in 1967 have tried to figure out the positions of hydrogen atoms in tetragonal H_xWO_{3-y} by neutron diffraction data. By comparing the relative intensities of a deuterium bronze and a hydrogen, they found that the H species in H_xWO_{3-y} are bound to O as an OH.[138] **Fig. 9** clearly illustrates the structural distortions of γ-monoclinic WO_3 induced by vacancies during the synthesis process. The W-W distance of perfect structure is 4.18 Å, which reduces to 3.72 Å due to the slight motion of W atoms to an Ov for the W vacancies (V_w) case. Along the body and face diagonals of the WO_6 unit cell, several locations are tested for possible interstitial sites. Compared with the W-O bond of 1.93 Å in perfect structure, W interstitial atom with a W-O bond of 2.08 Å is stable at the body centre (W_i). The body center (O_i-1) can be formed by an O interstitial atom, which can also lead to the formation of a W atom (O_i-2). A single O atom can bond to a H interstitial atom with a distance of 0.98 Å (H_i-1). This interstitial H atom that lies the face centre can bond to two O atoms with O-H distances of 1.67 Å and 1.01 Å (H_i-2). Eventually, another HO interstitial vacancy ($(HO)_i$) can form with H-O distance of 1.05 Å and 1.02 Å, which behaves similar to H_i-2. In the recent years, many groups have achieved great success in studying plasmonic H_xWO_{3-y} on synthesis methods and applications.[139]

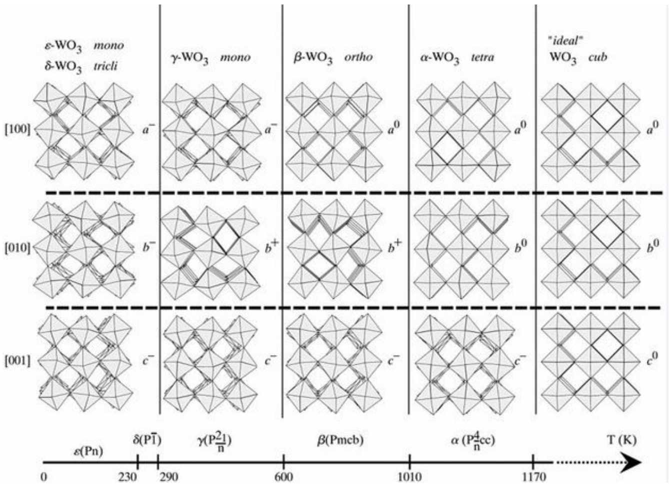

Fig. 8. Tilt patterns and stability temperature domains of the different polymorphs of WO_3. Reproduced with permission from Ref. [130]. Copyright 2019 Wiley-VCH.

2.4.1 Synthesis and Applications of H_xWO_{3-y} NCs.

Many methods for the synthesis of plasmonic H_xWO_{3-y} have been performed by both liquid- and vapor-phase-based routes.

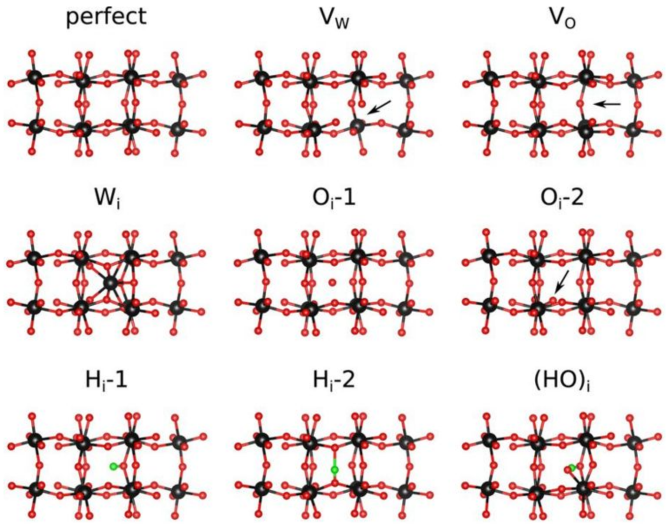

Fig. 9. Structures: Perfect, with vacancies, and with interstitial defects, refer to the text for details. W, O, and H atoms are shown in black, red, and green color, respectively. Reproduced with permission from ref. [35]. Copyright 2017 Springer Nature.

Hydrogen tungsten bronzes were firstly synthesized by Glemser et al. by passing suspensions of WO_3 in hydrochloric acid, in which the strength of the acid plays a vital role in controlling the composition of the product.[138,139] Subsequently, Boudart et al. reported that H_xWO_{3-y} was synthesized by hydrogen reduction of mixture of WO_3 and Pt black at 130 ^oC. In above study, nuclear magnetic resonance was used to further understand the kinetics of catalytic reduction of WO_3, which indicates that the penetration of reducing species is rate determining below the surface of WO_3 particles. After that, hydrogen reduction gradually becomes frequently-used method to synthesize plasmonic H_xWO_{3-y}. Urretavizcaya et al. reported that H_xWO_{3-y} was obtained through two steps. Cu/H_xWO_{3-y} was prepared by reducing a mixture of $CuWO_4$ under H_2 atmosphere and then Cu was washed away by concentrated HNO_3.[132] WO_3 as a photoanode material for photoelectrochemical water splitting has attracted a lot of interest owing to its favorable bandgap. However, as the peroxo-species lead to photocorrosion of WO_3 in water oxidation, photoelectrochemical instability is a primal problem for the WO_3 photoanode. By introduction of Ov, Li et al. proved that photocatalytic performance and stability of WO_3 after the reduction of hydrogen atmosphere at different temperatures can be simultaneously improved for water oxidation.[140] The increased stability of WO_3 is ascribed to the formation of substoichiometirc H_xWO_{3-y}, which strongly suppresses the re-oxidation and the formation of peroxo species. Zou et al. reported that H_xWO_{3-y} is an efficient and versatile catalyst for the hydrogenation of aryl nitro group, cyclic olefins, and linear olefins, which shows clear advantages in the aspect of selectivity and activity compared with non-noble Ni-catalyst.[141] First, they proved that H_2 can be easily activated by the surface Ov of WO_3 in kinetics and thermodynamics by using density functional theory (DFT) calculations.

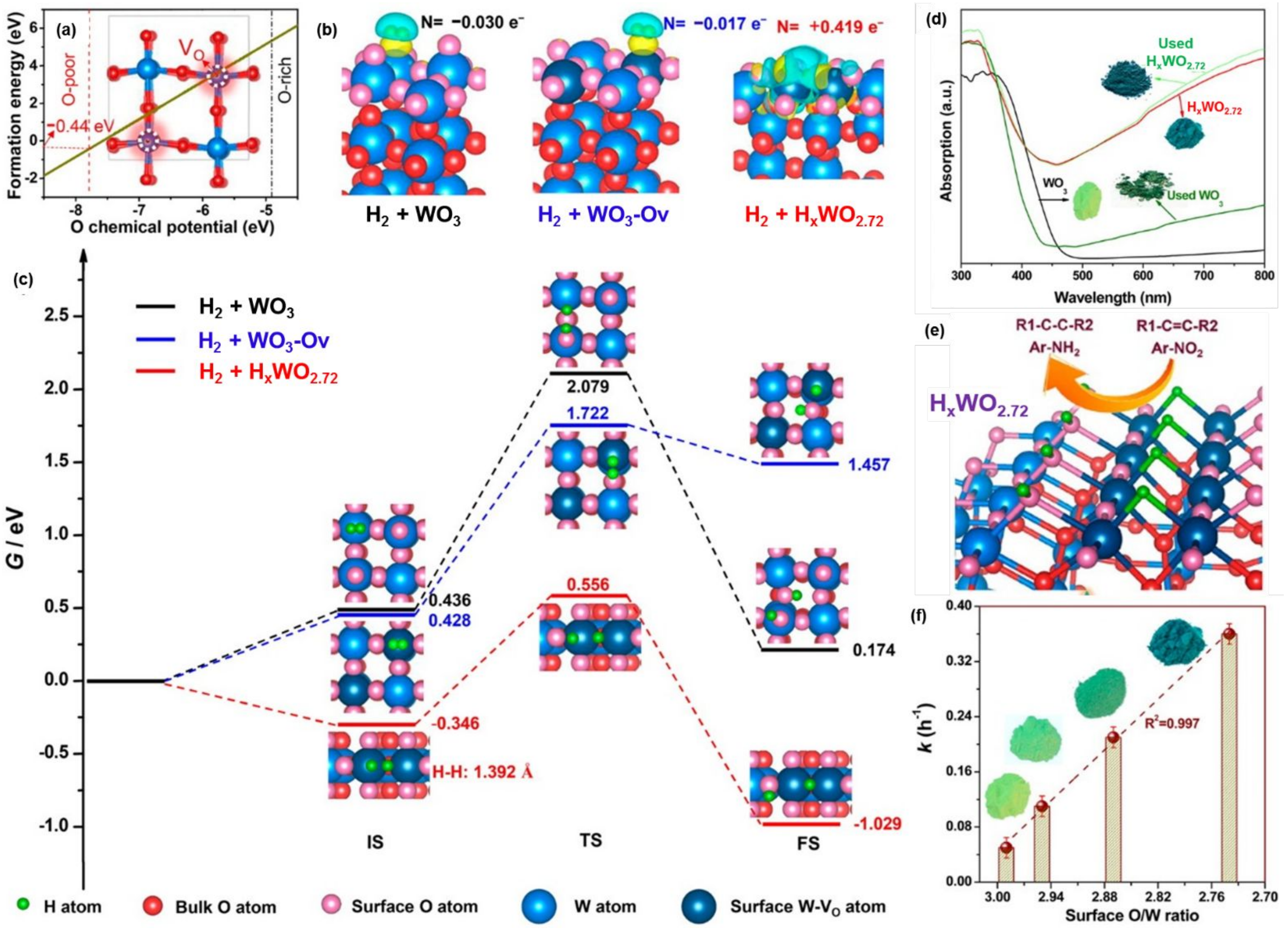

Fig. 10. a) Formation energy of WO_3-Ov surface under different O chemical potential (T = 0 K). (Inset: Top view of WO_3 surface with Ov. The dotted vertical lines indicate the allowed range of O chemical potential.) b) Differential charge density of H_2 adsorption. (The yellow and blue colors represent charge depletion and accumulation, respectively, with iso-surface value of 0.002 $eÅ^{-3}$. Number of electrons (N) represents the electron transferred from H_2 to catalyst, and plus (+) represents electron transferring from surface to H_2 while minus (−) represents the reverse). c) Free energies of the initial (IS), transition (TS), and final states (FS) for the dissociation of H_2. d) Diffuse reflectance spectra of H_xWO_{3-y} and WO_3. e) Diagram of nitrobenzene hydrogenation reaction. f) Linear correlation between initial reaction rate and oxygen vacancy concentration (surface O/W ratio). Reproduced with permission from Ref. [141]. Copyright 2015 American Chemical Society.

Three different surfaces, $H_xWO_{2.72}$ surface with abundant Ov, WO_3 surface with few Ov (WO_3-Ov), and stoichiometric WO_3 surface, are prepared to investigate the adsorption, activation, and dissociation of molecular H_2 (**Fig. 10**). **Fig. 10a** shows a modest propensity to form Ov under oxygen-poor conditions depending on the formation energy of -0.44 eV (T = 0 K). From **Fig. 10b-c**, it is observed that almost no H_2 can be activated (only 0.030 e^- shifted from H_2 to WO_3) and H_2 cannot be adsorbed (adsorption free energy of 0.436 eV). High barrier of 1.643 eV implies that the breaking of H-H bond is unfeasible in kinetics. On the contrary, a slight reduction occurs on both the energy barrier of H-H bond cleavage and the H_2 adsorption free energy (1.294 and 0.428 eV, respectively) for WO_3-Ov, which is much easier to activate H_2. Furthermore, one dissociated H atom bongs to a bridge atom and the other with a surface W atom, indicating the presence of Ov also change the manner of H_2 dissociation. Due to the adsorption free energy of -0.346 eV, the adsorption of H_2 is very easy on the surface of $H_xWO_{2.72}$. In addition, the H-H bond is elongated to 1.39 Å. By transferring 0.419 e^- to H_2, $H_xWO_{2.72}$ surface has a strong interaction with H_2. DFT calculations demonstrate that molecular H_2 is activated easily from the aspects of thermodynamics and kinetic by the Ov surface. In the UV-vis diffuse reflectance spectrum (**Fig. 10d**), the strong absorption tail dramatically illustrates the presence of Ov in H_xWO_{3-y}. Even after hydrogenation reaction of 1-hexene, the absorption intensity of H_xWO_{3-y} remains unchanged. As shown in **Fig. 10e-f**, a lower ratio of surface O/W leads to the quicker reaction process. More importantly, a very good correlation coefficient of 0.997 strongly indicates that the initial reaction rate is linearly with the surface O/W ratio. The above result obviously exhibits the unique Ov on the surface of $H_xWO_{2.73}$ governs the hydrogenation activity. In addition to thermal treatment in hydrogen atmosphere, other efficient synthesis methods of H_xWO_{3-y} were also adopted. For example, Lin et al. reported that surface Ov in WO_3 were prepared by an economical vacuum deoxidation and simple method, in which vacuum heat treatment temperature efficiently controls the concentration of oxygen vacancy. Comparing to the bulk defects, the surface Ov play a more crucial role in improving the photocatalytic performance of water oxidation under visible light irradiation.[142] A recent study by Ishihara et al. reported that H_xWO_{3-y} nanotubes with large amounts of surface Ov sites were synthesized by an oleate-assisted hydrothermal method,[15] which show highly efficient CO_2 reduction to CH_3COOH under solar light. Murray et al. reported that colloidal H_xWO_{3-y} NWs were synthesized by high temperature non-hydrolytic (solvothermal) reaction,[143] where WCl_6 as precursor was added into the mixture of 1-octadecenol and oleylamine. As-synthesized H_xWO_{3-y} NWs with Ov show a broad absorption from visible to NIR region. As a result of the Burstein-Moss shift, the optical band gap of H_xWO_{3-y} NWs is improved compared to that of pristine WO_3 powders. On account of this improvement, H_xWO_{3-y} NWs exhibit a direct and stable photocatalytic hydrogen evolution in photoreforming reactions using alcohols as electron donors. As we all know, H_xWO_{3-y} NCs have intense visible and NIR absorption. However, the optical absorption origin of H_xWO_{3-y} NCs is not unclear. For example, on the basis of photoluminescence and electrical transport studies, $WO_{2.72}$ NWs appear to be semiconducting and their blue color may arise from polaron hopping. On the contrary, on the basis of electrical transport measurements and XPS, $WO_{2.8}$ NWs seem to be metallic, but their blue color has not been discussed. Alivisatos et al. have made outstanding contribution in this field. They demonstrated that metallic phases of H_xWO_{3-y} NPs show a strong and tunable LSPRs.[24] H_xWO_{3-y} nanorods were synthesized under an inert atmosphere at 315 °C by hot injection of tungsten (V) ethoxide into a solvent mixture of trioctylamine acid and oleic acid.

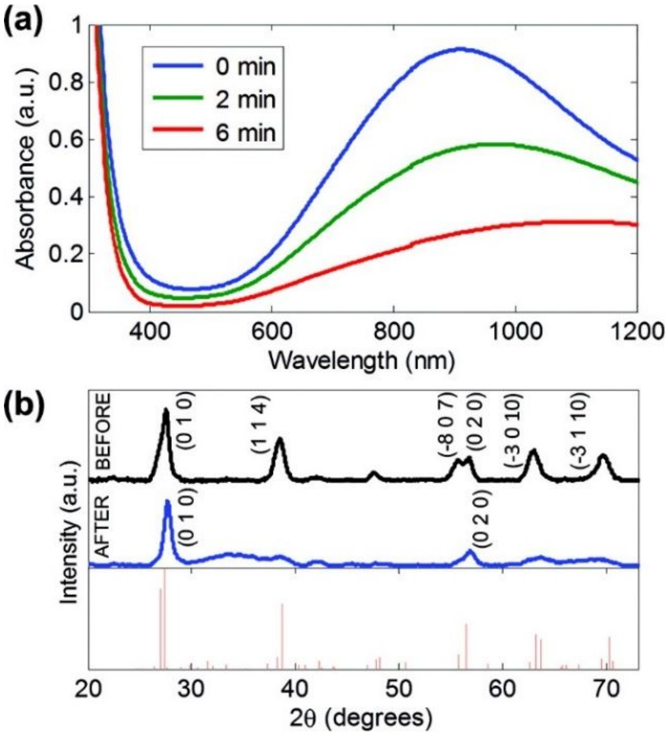

Fig. 11. a) UV–vis–NIR absorption spectra of H_xWO_{3-y} nanorods in N-methylpyrrolidone upon heating at 175 °C in air for 0, 2, and 6 min. b) XRD patterns of H_xWO_{3-y} nanorods in N-methylpyrrolidone (top) before and (middle) after heating at 175 °C for 6 min in air and (bottom) the reference pattern for H_xWO_{3-y}. Reproduced with permission from Ref. [24]. Copyright 2012 American Chemical Society.

The plasmon energy of such plasmonic H_xWO_{3-y} could be tuned by heating in air. It is observed a decrease in the intensity of the plasmonic absorption and a red shift while the solution of H_xWO_{3-y} in N-methylpyrollidone is heated at 175 °C in an oxidizing environment (**Fig. 11a**), which causes oxygen species to incorporate into the lattice, resulting in a decrease of the carrier concentration. Conversely, under an argon atmosphere, the same effect cannot arise when the solution is heated, indicating oxygen incorporation annihilates the charge carrier and then affects the shift of band-gap absorption under heating. The disordered structure of H_xWO_{3-y} after heating is observed by XRD (**Fig. 11b**), which demonstrates that crystallinity is fully retained when oxygen is inserted into the structure at a low temperature.[24] Sunlight-driven chemical transformation by metal oxides hold a great promise for catalyst cost and a substantial reduction in energy consumption. However, the step of energy transfer from excitons to dioxygen species remains a grand challenge to energy coupling. Xiong et al. demonstrated that WO_3 with abundant Ov can approach the above challenge, which insures the chemisorption of molecular oxygen to WO_3 surface. In addition, it is quite interesting that the Ov in tungsten oxide could be also introduced by air treatment,[142] which was confirmed by XPS and ESR spectra. The above production of Ov is attributed to two mechanisms, i.e., nanoscale inhomogeneous and critical phase transition, which depends on the size of the building block and annealing time or temperature. For comparison, the Ov are also introduced by hydrogen reduction by Tang et al.. Ov induced by hydrogen treatment can boost recombination of the electron-hole pair, which leads to lower electrochemical performance and photocatalytic activity. However, Ov induced by air treatment can capture and shift electrons, which decreases the recombination rate of electron-hole pair. In conclusion, considering the opposite results on oxygen defects of H_xWO_{3-y}, there is still a lot of space for accurately understanding the formation of oxygen defects in the future.

2.4.2 Synthesis and Applications of H_xWO_{3-y} Hybrids

Noble metal/plasmonic semiconductor NCs hybrids have attracted great interest owing to their wide applications in catalysis. H_xWO_{3-y} NCs with strong LSPRs absorption offer a big chance to realize high catalytic performance by depositing metal NPs onto their surfaces. In this case, it would be better to improve the selectivity and conversion of chemical reactions by taking advantage of LSPRs excitation of H_xWO_{3-y}, which is catalyzed by the deposited metal NPs. For example, Xue et al. reported that the deposition of Pd NPs on the surface of plasmonic H_xWO_{3-y} NWs with strong LSPRs absorption dramatically enhances the Suzuki coupling reaction under long wavelength (λ > 650nm) catalyzed by Pd NPs.[144] During the synthetic process, $W(CO)_6$ as precursor and ethanol as solvent were used to prepare H_xWO_{3-y} NWs by solvothermal treatment at 160 °C for 12 h. After that, Pd/H_xWO_{3-y} NWs were synthesized by depositing Pd NPs on the surface of H_xWO_{3-y} with $NaBH_4$ as a reductant. Ravikumar et al. found that platinized carbon electrodes without H_xWO_{3-y} show worse catalytic performance for methanol electrooxidation than the electrodes containing Pt/H_xWO_{3-y} composite.[145] Based on the XPS and XRD data, H_xWO_{3-y} NCs are presented in the form of an oxyhydroxide (W-OH), in which the promotional performance of plasmonic H_xWO_{3-y} is concerned with the W(VI)/W(IV) redox couple serving as a surface mediator for the oxidation of surface methanolic residues. Yu et al. have synthesized Pd/H_xWO_{3-y} composite by a novel and surfactant-free method, where H_xWO_{3-y} NWs with Ov supply free electrons to reduce Pd^{2+} in aqueous solution by an *in situ* redox reaction between Pd^{2+} and reductive H_xWO_{3-y}. Such plasmonic Pd/H_xWO_{3-y} hybrid exhibits a high catalytic performance for the reduction of styrene and *p*-nitrophenol, where Ov NWs can quickly transfer electrons from the surface of H_xWO_{3-y} to Pd NPs and accelerate hydrogen adsorption and dissociation.[146] From the above studies, it is of great significance to develop rational methods without surfactant to plasmonic metal/H_xWO_{3-y} hybrid, which could ensure the catalysts surfaces completely avoid impurities and provide the versatile synthetic alternative. Zhao et al. reported a recyclable, stable, and clean 3D chestnut-like Ag/$H_xWO_{2.72}$ nanostructures (CSWNs) surface-enhanced Raman scattering (SERS) substrate, which was developed by a hydrothermal reaction and a subsequent facile *in situ* redox of Ag species at room temperature.[147] The unique recyclable capability of SERS substrate supported by the decoration of Ag NPs on the surface of H_xWO_{3-y} is successfully realized by photocatalytic degradation of thiram. Obviously, the detection limit down to 0.32 nM is achieved by the CAWNs SERS substrates in **Fig. 12a**. More importantly, by the detection of thiram in spiked fruits peels (such as orange and carambola), the real-life application is also performed successfully by using the SERS-active CAWNs colloid (**Fig. 12b**). From the signal analysis of Raman spectra, two dimethylthiocarbamate fragments are generated under laser irradiation by the break of the S-S bond of thiram molecules. The innovative design combines self-cleaning property and the SERS enhancement effect for highly sensitive SERS detection, which provides a reusable and multifunctional SERS platform.[147] In addition, alternative catalysts avoiding noble metals are highly demanded due to their earth rarity and high resistive loss.

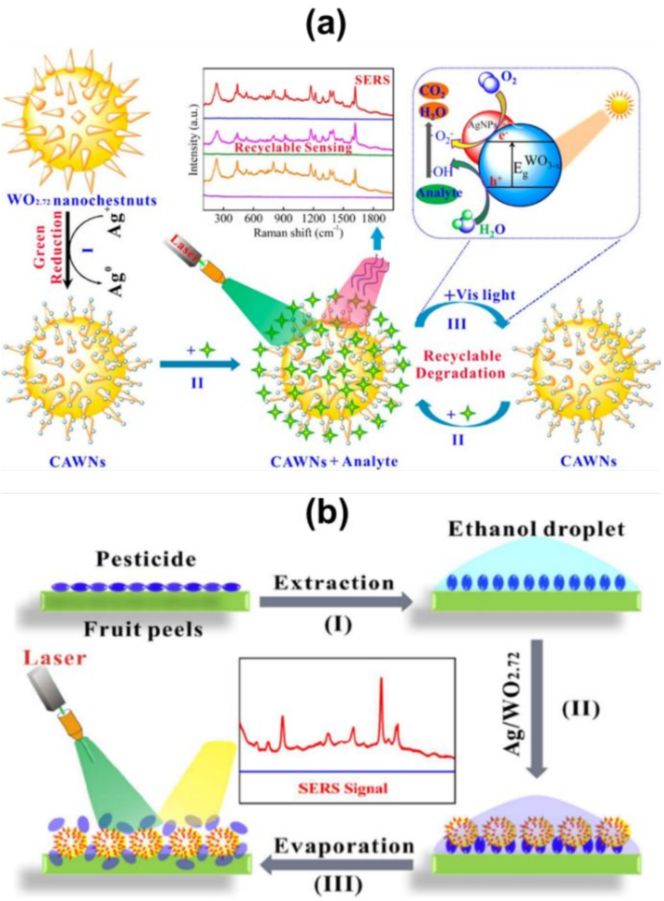

Fig. 12. a) Schematic illustration of the fabrication process of the 3D recyclable chestnut-like Ag/$H_xWO_{2.72}$ nanostructures and its application: (I) Ag NPs decorated on $H_xWO_{2.72}$ nanochestnuts, (II) analyte loading and SERS sensing, and (III) the regeneration of recyclable SERS substrates. b) Schematic illustration of the practical detection of pesticide residuals in fruits peels by using the as-prepared Ag/H_xWO_{3-y} colloid. Reproduced with permission from Ref. [147]. Copyright 2017 American Chemical Society.

Photocatalytic hydrogen production through water splitting is seen as environmentally friendly method. Herein, Yousaf et al. developed an efficient Z-Scheme photocatalytic system consisting of oxygen deficient H_xWO_{3-y} nanorods and $Zn_{0.3}Cd_{0.7}S$ NPs, which exhibits a high photocatalytic H_2 evolution rate (352.1 μmol h^{-1}) with apparent quantum efficiency (AQY) of 7.3% at λ = 420 nm. Compared to $WO_3/Zn_{0.3}Cd_{0.7}S$, $H_xWO_{3-y}/Zn_{0.3}Cd_{0.7}S$ heterostructure with Ov shows considerably higher overall hydrogen evolution rate without noble metals. The strong interface contact between $Zn_{0.3}Cd_{0.7}S$ NPs and H_xWO_{3-y} nanorods makes positive contribution to the migration of electrons. The strong absorption induced by H_xWO_{3-y} nanorods favors the enhancement of the activity in the visible region. In preparation for $H_xWO_{3-y}/Zn_{0.3}Cd_{0.7}S$ heterostructure, H_xWO_{3-y} nanorods were synthesized by H_2 reduction of WO_3 after hydrothermal method and subsequent $H_xWO_{3-y}/Zn_{0.3}Cd_{0.7}S$ was prepared by adjusting the pH of the solution of $Cd(CH_3COO)_2$, $Zn(CH_3COO)_2$ and Na_2S.[148] Chen et al. reported that a facile two-step synthetic route was used to prepare H_xWO_{3-y}/C NWs with abundant Ov, involving ammonium tetrathiotungstate ($(NH_4)_2WS_4$) and dopamine as the precursors. As-synthesized free-standing H_xWO_{3-y}/C NWs demonstrate outstanding performance for H_2 generation and show fairly high stability without significant current density drop even after 1000 cycles.[149]

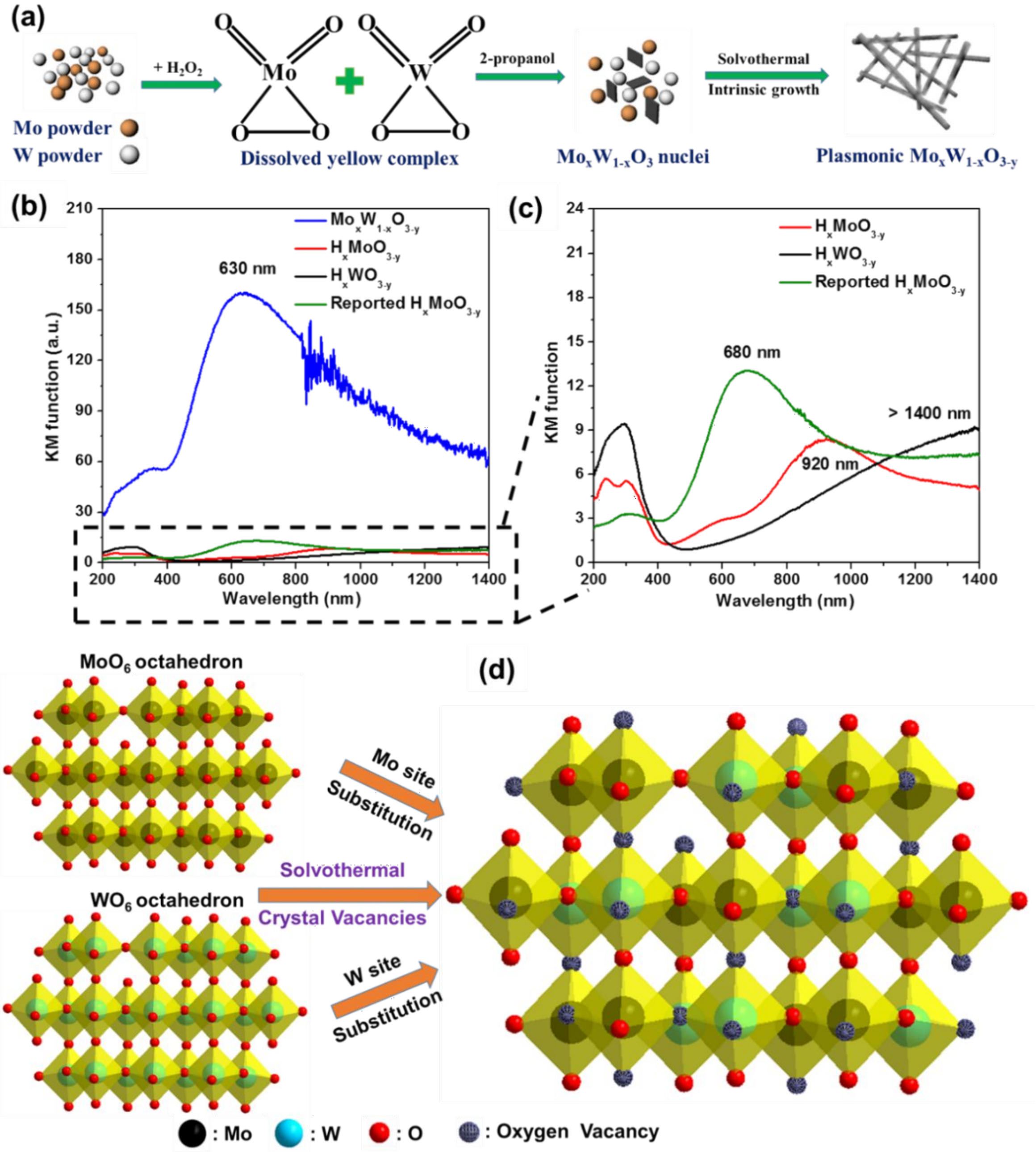

Fig. 13. a) Schematic illustration of the plausible formation process of plasmonic $Mo_xW_{1-x}O_{3-y}$. b) UV–vis-NIR diffuse reflectance spectra of $Mo_xW_{1-x}O_{3-y}$, H_xMoO_{3-y}, H_xWO_{3-y}, and our previously reported H_xMoO_{3-y} nanosheets. c) Magnified UV–vis-NIR diffuse reflectance spectra of H_xMoO_{3-y}, H_xWO_{3-y}, and our previously reported H_xMoO_{3-y} nanosheets in b). d) Illustration of the possible formation process of crystal defects in plasmonic $Mo_xW_{1-x}O_{3-y}$ structure. Reproduced with permission from Ref. [152]. Copyright 2017 American Chemical Society.

To meet the demand of developing clean-energy technologies, preparation of highly earth-abundant, stable, and active photoanodes for water oxidation is a crucial step. For example, Zhang et al. reported that stable and efficient black H_xWO_{3-y}/TiO_{2-x} core-shell nanosheets photoanodes were synthesized by H_2 reduction for photoelectrochemical (PEC) conversion. Compared to a pure WO_3 photoanode, such H_xWO_{3-y}/TiO_{2-x} photoanode shows 8 times higher photocurrent density at the same condition. By electrochemical spectroscopic, specific band alignment, and finite-difference time-domain evidence, the high PEC water oxidation activity is attributed to charge separation and transfer, and light absorption in these H_xWO_{3-y}/TiO_{2-x} nanosheets. Furthermore, the H_xWO_{3-y}/TiO_{2-x} photoanodes display a good photostability even after continuous PEC water splitting experiment for 6 h.[150] Construction of 1D/2D heterostructure is a new type and has aroused great interest. For example, Xue et al. have constructed a 1D/2D $H_xWO_{3-y}/g\text{-}C_3N_4$ heterojunction through a simple solvothermal method, where H_xWO_{3-y} NWs are growing on the surface of $g\text{-}C_3N_4$ nanosheets. Such hybrid shows high photocatalytic activities for the degradation of methyl orange (MO), which is ascribed to effective electron transfer from excited $g\text{-}C_3N_4$ to H_xWO_{3-y} NWs. The improved photocatalytic performance over the $H_xWO_{3-y}/g\text{-}C_3N_4$ hybrid results from the abundant Ov in H_xWO_{3-y}, which leads to a great number of free electrons on H_xWO_{3-y} nanowires. The surface of large nanowires with strong conductivity and capability for O_2 adsorption drives the injected electrons to reduce these O_2 and produce superoxide radicals for the degradation of MO. Although the research of the hydrogen tungsten bronze hybrids has achieved some breakthroughs, greater efforts should be made to further seriously study and fully use of the plasmonic effect.

2.5 Non-stoichiometric $Mo_xW_{1-x}O_{3-y}$ and $Mo_xW_{1-x}O_{3-y}$ hybrid

Molybdenum and tungsten elements have the same number of electrons in the outermost layer, which belong to group VI elements in the periodic table. Moreover, the metallic phases of both H_xMoO_{3-y} and H_xWO_{3-y} NCs exhibit tunable and strong LSPRs, which provides an opportunity of rationally designing plasmonic $Mo_xW_{1-x}O_{3-y}$ for bioimaging, sensing, and light harvesting.[148] A synthesis of new-type plasmonic NCs with intense light absorption property is expected to be achievable by coupling of H_xMoO_{3-y} and H_xWO_{3-y} NCs. For example, Yamashita et al. reported that plasmonic $Mo_xW_{1-x}O_{3-y}$ hybrid with strong LSPRs in the visible light region was synthesized by a facile non-aqueous solvothermal method without adding any surfactants.[152] During the synthesis of plasmonic $Mo_xW_{1-x}O_{3-y}$ hybrid (**Fig. 13a**), molybdenum metal powders and tungsten metal powder were dissolved by H_2O_2 in 2-propanol and subsequently the obtained yellow suspension was added in Teflon vessel for solvothermal treatment. The solution-soluble precursor compound $WO_2(OH)(OOH)$ and $MoO_2(OH)(OOH)$ can firstly form in this process. By dehydration of the dissolved yellow Mo-W-complex in the growth stage, tiny $Mo_xW_{1-x}O_{3-y}$ nuclei are generated. With the help of 2-propanol, the intrinsic anisotropic crystal growth results in the preferential formation of $Mo_xW_{1-x}O_{3-y}$ NWs. The formation mechanism is based on the layered crystal structure of orthorhombic WO_3 and MoO_3 composed of WO_6 octahedra and MoO_6 octahedra sharing edges and corners, respectively. In the UV-vis-NIR spectra (**Fig. 13b-c**), this $Mo_xW_{1-x}O_{3-y}$ hybrid shows a strong absorption peak located at around 630 nm, which connects with LSPRs. In plasmonic semiconductors, such a strong LSPR peak is infrequent in visible light range, even in the NIR or MIR region. Also, the absorption peak position (630 nm) of $Mo_xW_{1-x}O_{3-y}$ is shorter than that of previously reported H_xMoO_{3-y} (680 nm) nanosheets, as-synthesized H_xWO_{3-y} (>1400 nm), and H_xMoO_{3-y} (920 nm). It is amazing that plasmonic peak strength of $Mo_xW_{1-x}O_{3-y}$ is around 8, 16, and 20 times higher than that of previously reported H_xMoO_{3-y} nanosheets, as-synthesized H_xWO_{3-y}, and H_xMoO_{3-y}, respectively. It is proved that LSPRs are formed from crystal vacancies, mainly containing oxygen defects and mutual doping defects of molybdenum ions and tungsten ions (**Fig. 13d**). Similar phenomenon was also observed by Xiong et al..[151]

Recently, some researchers have already reported the importance of Ov in ammonia synthesis process. Zhang' s group first reported that Ov with abundant localized electrons on the surface of the BiOBr nanosheets can remarkably promote the adsorption and activation of N_2 and improve the reduction efficiency of N_2 to NH_3 under atmospheric pressure and room temperature by visible light irradiation. However, surface Ov are easily oxidized by the h^+ in valence band (VB) during the reaction. Therefore, robust semiconductors with abundant and sustainable Ov that efficiently promote water oxidation and N_2 reduction are necessary. Xiong et al. demonstrated that this bottleneck was solved by refining the vacancy states with doping in photocatalysts.[153] $Mo_xW_{1-x}O_{3-y}$ ultrathin NWs are synthesized through a mild solvothermal method with ethanol as solvent and WCl_6 and $MoCl_5$ as precursors. In plasmonic $Mo_xW_{1-x}O_{3-y}$ with oxygen defects, the coordinatively unsaturated (CUS) metal atoms act as the active sites for electron transfer and N_2 chemisorption. In facilitating N_2 activation and dissociation, the doped low-valence Mo species play multiple crucial roles. On the one hand, they can boost the electron transfer from CUS sites to absorbed N_2 and polarize the absorbed N_2 molecules. On the other hand, the energy of photoexcited electrons for N_2 reduction is sufficient because they can promote vacancy-band center to the Fermi level. The high-resolution W 4f XPS spectra show that both W^{4+}, W^{5+}, and W^{6+} are appeared in the H_xWO_{3-y} and $Mo_xW_{1-x}O_{3-y}$ (**Fig. 14a**). The valence state of W is not varied by Mo doping, which is proved by the similar fitting results for H_xWO_{3-y} and $Mo_xW_{1-x}O_{3-y}$. In principle, the low-valence W species (i.e., W^{4+} and W^{5+}) should be described by the eqn (1):

$$2W^{6/5+} + O^{2-} \rightarrow 2W^{5/4+} + O + Ov \qquad (1)$$

where O^{2-}, Ov, and O is the lattice oxygen, oxygen vacancy, and the removed oxygen, respectively. Excessive electrons are left in the lattice by the removal of lattice oxygen. In this case, the generation of low-valence W species are concomitant with oxygen vacancy, which leads to the strong light absorption in visible and NIR region. In addition, two peaks (at 234.7 and 231.6 eV) are attributed to the Mo^{6+} species of $Mo_xW_{1-x}O_{3-y}$ (**Fig. 14b**). ESR spectrum of $Mo_xW_{1-x}O_{3-y}$ NWs shows a hyperfine structure with both perpendicular ($g_{\perp}$ = 1.907) and parallel ($g_{|}$ = 1.846) bands (**Fig. 14c**). The g values display the existence of Mo-O tetragonal pyramids. Furthermore, the doped Mo species are coordinately unsaturated, which was demonstrated by the penta-coordination. It displays that electrons do not delocalize over the lattice but they are trapped by Mo^{5+} atoms in consideration of the absence of signal at g = 2.003 for free electrons, which is shown from the structure illustration for the lattice of vacancy-rich in $Mo_xW_{1-x}O_{3-y}$ (**Fig. 14d**). However, compared to plasmonic H_xMoO_{3-y} and H_xWO_{3-y}, the photocatalytic performance of $Mo_xW_{1-x}O_{3-y}$ for some catalytic reactions (such as the dehydrogenation of NH_3BH_3 or N_2 fixation) does not enhance much. Based on the above discussion on heterogeneous photocatalysis for improving catalytic performance, it is crucial and intriguing to synthesize plasmonic $Mo_xW_{1-x}O_{3-y}$ hybrids. Yamashita et al. developed a solution-processed method to prepare a plasmonic Pd/$Mo_xW_{1-x}O_{3-y}$ hybrid by coupling a $Mo_xW_{1-x}O_{3-y}$ and Pd NPs during the reduction process with $NaBH_4$ as a reductant (**Fig. 15a**).[76] The above plasmonic hybrid show very strong LSPRs from the visible to the NIR (**Fig. 15b**). Under visible light irradiation, the synthesized Pd/$Mo_xW_{1-x}O_{3-y}$ hybrid shows dramatic H_2 production activity enhancement from NH_3BH_3 solution, which is mainly attributed to the synergetic effect between W^{5+} ions and Pd NPs. Furthermore, the activity of Pd/$Mo_xW_{1-x}O_{3-y}$ hybrid is almost 5 and 5.2 times higher than those of previously reported Pd/H_xMoO_{3-y} nanosheets and $Mo_xW_{1-x}O_{3-y}$ **(Fig. 15c-e)**. It will undoubtedly have a place in this field in the near future with its excellent plasma effect.

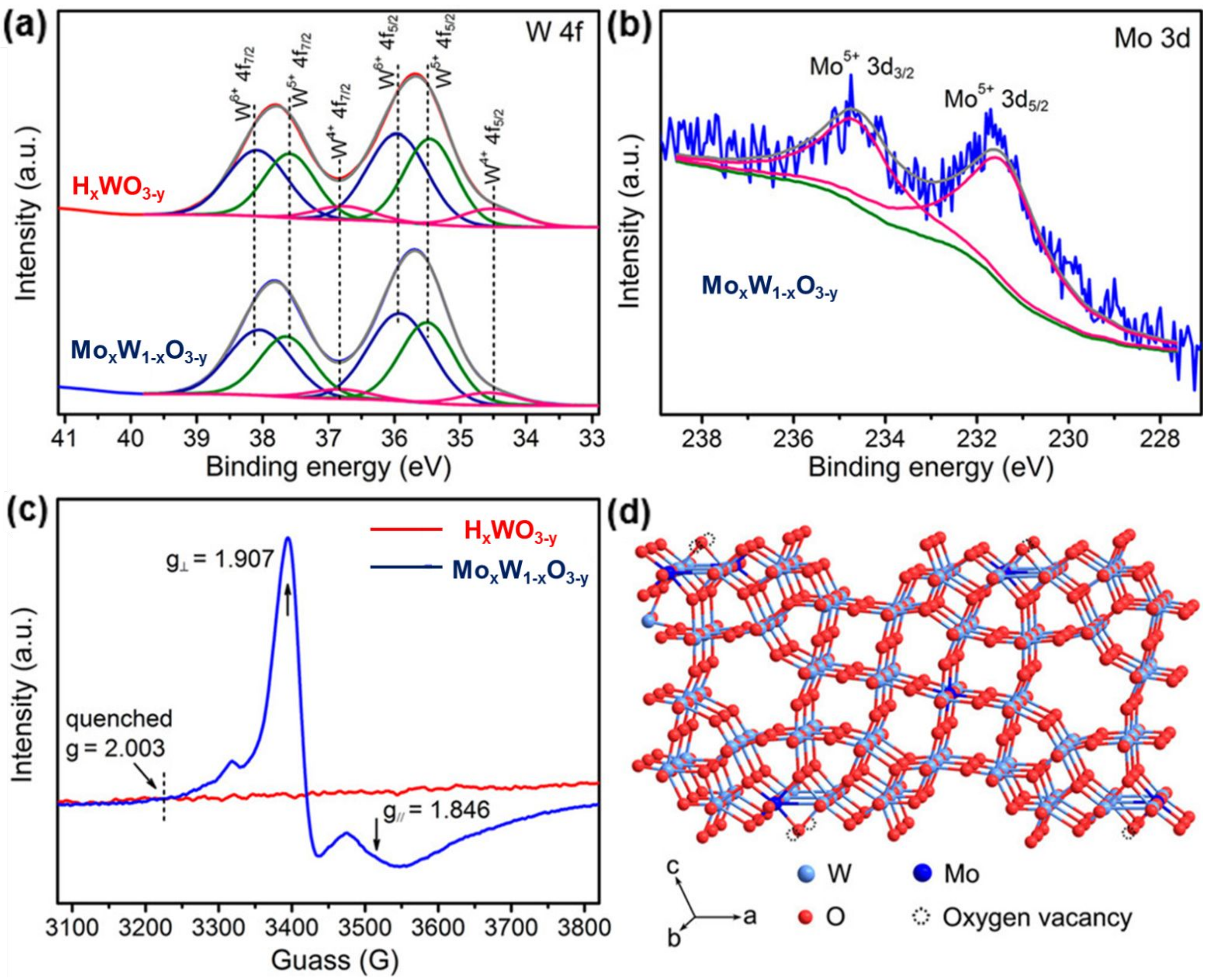

Fig. 14. Structural characterizations for as-prepared H_xWO_{3-y} and $Mo_xW_{1-x}O_{3-y}$ NWs. High-resolution (a) W 4f and (b) Mo 3d XPS spectra. (c) ESR spectra at 140 K. (d) Structural illustration for the lattice of defect-rich $Mo_xW_{1-x}O_{3-y}$ NWs. Reproduced with permission from Ref. [150]. Copyright 2018 American Chemical Society.

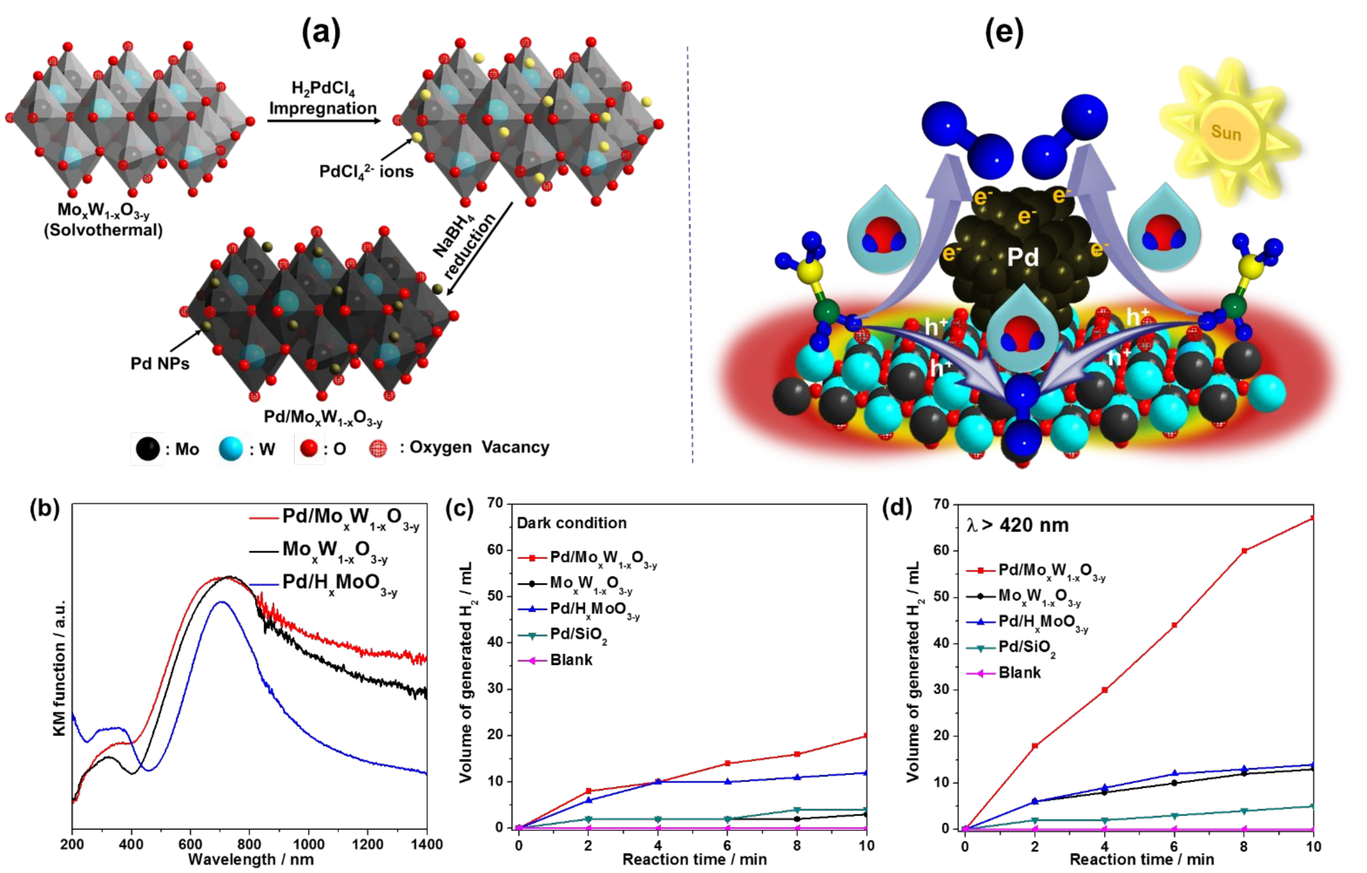

Fig. 15. a) Schematic illustration of the synthesis procedure of the $Pd/Mo_xW_{1-x}O_{3-y}$ hybrid. UV-Vis-NIR diffuse reflectance spectra of b) $Pd/Mo_xW_{1-x}O_{3-y}$ and reference samples. The plot of evolved H_2 gas as a function of reaction time from an aqueous NH_3BH_3 solution (1 mmol in 10 mL water) hydrolysis over different catalysts c) in the dark, d) under visible light irradiation (λ > 420 nm) within 10 min. e) Illustration of NH_3BH_3 dehydrogenation reaction over $Pd/Mo_xW_{1-x}O_{3-y}$ hybrid. Reproduced with permission from Ref. [76]. Copyright 2018 Royal Society of Chemistry.

3. Summary and Outlook

The origins and developments of plasmonic semiconductors NCs (especially molybdenum bronze and tungsten bronze) have been described in detail. Fundamentals, main synthesis methods, and main applications of H_xMoO_{3-y} (hybrids), H_xWO_{3-y} (hybrids), and $Mo_xW_{1-x}O_{3-y}$ (hybrids) have been presented.

1. H_xMoO_{3-y} (hybrids)

The main synthesis methods of plasmonic H_xMoO_{3-y} (hybrid) are hydrothermal, solvothermal method (high temperature non-hydrolytic reaction), templating and surfactant methods, exfoliation method, H_2 plasma etching, H_2 thermal reduction, $NaBH_4$ chemical reduction and so on. According to the above discussion, the intercalated H^+ cations mainly bind to terminal oxygen atoms and edge-shared oxygen in the H_xMoO_{3-y} structure. The intercalated H^+ cations can reduce bandgap and expand the van der Waals gap. The plasmonic absorption of H_xMoO_{3-y} can be also tuned according to the H^+ concentration that depends on the preparation conditions, such as temperature of H_2 reduction, the concentration of reductants and so on. H_xMoO_{3-y} (hybrids) shows dramatically enhanced photocatalytic activity, especially in the dehydrogenation of ammonia borane and the reduction of *p*-nitrophenol, as well as extraordinary high sensitivity on surface-enhanced Raman scattering detection.

2. H_xWO_{3-y} (hybrids)

Similarly, the intercalated H^+ cations mainly bind to oxygen atoms of the H_xWO_{3-y} structure. The primary methods of plasmonic H_xWO_{3-y} (hybrids) synthesis are also H_2 thermal reduction, $NaBH_4$ chemical reduction, high temperature non-hydrolytic (solvothermal) reaction, hot injection of tungsten (V) ethoxide and so on. The plasmonic properity of H_xWO_{3-y} (hybrids) can be also changed by tuning reaction conditions. Furthermore, H_xWO_{3-y} (hybrids) exhibits drastic increase~~d~~ in photocatalytic performance, such as the hydrogenation of aryl nitro group, cyclic olefins, and linear olefins, the Suzuki coupling, photocatalytic CO_2 reduction and so on.

3. $Mo_xW_{1-x}O_{3-y}$ (hybrids).

Up to now, the most frequently used and simple methods for the preparation of $Mo_xWO_{1-x}O_{3-y}$ is a solvothermal method. As-synthesized $Mo_xWO_{1-x}O_{3-y}$ (hybrids) is used to photocatalytic dehydrogenation of ammonia borane, photocatalytic N_2 reduction and so on.

In order to reach the desired outcomes, the review also displays how LSPRs of each plasmonic NCs could be controlled and tuned owing to the synthetic methods. Heavily-doped semiconductor NCs that show LSPRs is a relatively new and rapidly-developing research field. A potential alternative to metal NPs in some applications is presented by this group of novel plasmonic NCs, and new applications are also developed at NIR and MIR wavelengths due to the absorbance of NCs. At present, most work in this field focused on exploring methods for preparing high-quality NCs, developing new types of plasmonic semiconductors NCs, and essentially studying the optical properties of these semiconductors NCs for varied applications. The potential advantages of these NCs with tunable LSPRs also need to be further assessed, and the synthesis of semiconductor NCs must be optimized to better exploit these advantages. The purpose of this tutorial review is to compare synthetic methods and the applications of a variety of materials, summarizing key aspects of this research field. We hope this review will impel researchers to enter this research area. For practical applications of these novel types of plasmonic NCs, we still need to make a great amount of work with great energy.

Conflicts of interest

There are no conflicts to declare.

Acknowledgements

The present work was supported by the Grant-in-Aid for Scientific Research from the Ministry of Education, Culture, Sports, Science and Technology (MEXT) of Japan (No. 26220911 and 19H00838) and JST, PRESTO (No. JPMJPR19T3). A part of this work was supported by Element Strategy Initiative of MEXT, Japan (no. JPMXP0112101003).

Notes and references

1. J. N. Anker, W. P. Hall, O. Lyandres, N. C. Shah, J. Zhao and R. P. Van Duyne, in *Nanoscience and Technology*, Co-Published with Macmillan Publishers Ltd, UK2009, pp. 308-319.
2. K. A. Willets and R. P. Van Duyne, *Annu. Rev. Phys. Chem.*, 2007, **58**, 267-297.
3. M. Hu, J. Chen, Z.-Y. Li, L. Au, G. V. Hartland, X. Li, M. Marquez and Y. Xia, *Chem. Soc. Rev.*, 2006, **35**, 1084-1094.
4. J.M. Luther, P.K. Jain, T. Ewers and A.P. Alivisatos, *Nat. Mater.*, 2011, **10**, 361-366.
5. B. R. Cooper, H. Ehrenreich and H. R. Philipp, *Phys. Rev.*, 1965, **138**, A494-A507.
6. I. Kriegel, F. Scotognella and L. Manna, *Phys. Rep.*, 2017, **674**, 1-52.
7. A. Comin and L. Manna, *Chem. Soc. Rev.*, 2014, **43**, 3957-3975.
8. Y. Zhao, H. Pan, Y. Lou, X. Qiu, J. Zhu, C. Burda, *J. Am. Chem. Soc.*, 2009, **131**, 4253-4261.
9. J. Owen, *Science*, 2015, **347**, 615-616.
10. U. R. Kortshagen, R. M. Sankaran, R. N. Pereira, S. L. Girshick, J. J. Wu and E. S. Aydil, *Chem. Rev.*, 2016, **116**, 11061-11127.
11. R. Buonsanti and D. J. Milliron, *Chem. Mater.*, 2013, **25**, 1305-1317.
12. T.-L. Ho, *Chem. Rev.*, 1975, **75**, 1-20.
13. C. Wu, A. B. Khanikaev, R. Adato, N. Arju, A. A. Yanik, H. Altug and G. Shvets, *Nat. Mater.*, 2011, **11**, 69-75
14. A. Genç, J. Patarroyo, J. Sancho-Parramon, R. Arenal, M. Duchamp, E. E. Gonzalez, L. Henrard, N. G. Bastús, R. E. Dunin-Borkowski, V. F. Puntes and J. Arbiol, *ACS Photonics*, 2016, **3**, 770-779.
15. S. Sun, M. Watanabe, J. Wu, Q. An, and T. Ishihara, *J. Am. Chem. Soc*, 2018, **140**, 6474-6482.
16. Y. Shen, J. Zhou, T. Liu, Y. Tao, R. Jiang, M. Liu, G. Xiao, J. Zhu, Z.-K. Zhou, X. Wang, C. Jin and J. Wang, *Nat. Commun.*, 2013, **4**, 2381-2389
17. A. V. Kabashin, P. Evans, S. Pastkovsky, W. Hendren, G. A. Wurtz, R. Atkinson, R. Pollard, V. A. Podolskiy and A. V. Zayats, *Nat. Mater.*, 2009, **8**, 867-871
18. R. L. Olmon, B. Slovick, T. W. Johnson, D. Shelton, S.-H. Oh, G. D. Boreman and M. B. Raschke, *Phys. Rev. B*, 2012, **86**, 235147-235156.
19. H. U. Yang, J. D'Archangel, M. L. Sundheimer, E. Tucker, G. D. Boreman and M. B. Raschke, *Phys. Rev. B*, 2015, **91**, 235137-235147.
20. B. Auguié and W. L. Barnes, *Phys. Rev. Lett.*, 2008, **101**, 143902-143905.
21. A. M. Schimpf, K. E. Knowles, G. M. Carroll and D. R. Gamelin, *Acc. Chem. Res.*, 2015, **48**, 1929-1937.
22. Y. Liu, M. Liu and M. T. Swihart, *J. Phys. Chem. C*, 2017, **121**, 13435-13447.
23. A. M. Schimpf, S. T. Ochsenbein, R. Buonsanti, D. J. Milliron and D. R. Gamelin, *ChemComm.*, 2012, **48**, 9352-9354.
24. K. Manthiram and A. P. Alivisatos, *J. Am. Chem. Soc.*, 2012, **134**, 3995-3998.
25. A. M. Schimpf, C. E. Gunthardt, J. D. Rinehart, J. M. Mayer and D. R. Gamelin, *J. Am. Chem. Soc.*, 2013, **135**, 16569-16577.
26. J. D. Rinehart, A. M. Schimpf, A. L. Weaver, A. W. Cohn and D. R. Gamelin, *J. Am. Chem. Soc.*, 2013, **135**, 18782-18785.
27. D. Dorfs, T. Härtling, K. Miszta, N. C. Bigall, M. R. Kim, A. Genovese, A. Falqui, M. Povia and L. Manna, *J. Am. Chem. Soc.*, 2011, **133**, 11175-11180.
28. S. C. Erwin, L. Zu, M. I. Haftel, A. L. Efros, T. A. Kennedy and D. J. Norris, *Nature*, 2005, **436**, 91-94.
29. V. Giannini, A.I. Fernández-Domínguez, S.C. Heck and S.A. Maier, *Chem. Rev.*, 2011, **111**, 3888-3912.

30. S. Kalusniak, S. Sadofev and F. Henneberger, *Phys. Rev. Lett.*, 2014, **112**, 137401-137405.
31. R. J. Mendelsberg, G. Garcia and D. J. Milliron, *J. Appl. Phys.*, 2012, **111**, 063515-063518.
32. J. Kim, A. Agrawal, F. Krieg, A. Bergerud and D. J. Milliron, *Nano Lett.*, 2016, **16**, 3879-3884.
33. E. L. Runnerstrom, A. Bergerud, A. Agrawal, R. W. Johns, C. J. Dahlman, A. Singh, S. M. Selbach and D. J. Milliron, *Nano Lett.*, 2016, **16**, 3390-3398.
34. D. J. Rowe, J. S. Jeong, K. A. Mkhoyan and U. R. Kortshagen, *Nano Lett.*, 2013, **13**, 1317-1322.
35. J. Zhu, M. Vasilopoulou, D. Davazoglou, S. Kennou, A. Chroneos and U. Schwingenschlögl, *Sci. Rep.*, 2017, **7**, 40882-40891.
36. K. A. Fichthorn, *J. Chem. Eng. Data*, 2014, **59**, 3113-3119.
37. N. T. K. Thanh, N. Maclean and S. Mahiddine, *Chem. Rev.*, 2014, **114**, 7610-7630.
38. Y. Xia, X. Xia and H.-C. Peng, *J. Am. Chem. Soc.*, 2015, **137**, 7947-7966.
39. M. Sluydts, K. De Nolf, V. Van Speybroeck, S. Cottenier and Z. Hens, *ACS Nano*, 2016, **10**, 1462-1474.
40. A. J. Morris-Cohen, M. Malicki, M. D. Peterson, J. W. J. Slavin and E. A. Weiss, *Chem. Mater.*, 2013, **25**, 1155-1165.
41. X. Liu, X. Wang, B. Zhou, W.-C. Law, A. N. Cartwright and M. T. Swihart, *Adv. Funct. Mater.*, 2013, **23**, 1256-1264.
42. I. Kriegel, C. Jiang, J. Rodríguez-Fernández, R. D. Schaller, D. V. Talapin, E. da Como and J. Feldmann, *J. Am. Chem. Soc.*, 2012, **134**, 1583-1590.
43. W. Li, R. Zamani, P. Rivera Gil, B. Pelaz, M. Ibáñez, D. Cadavid, A. Shavel, R. A. Alvarez-Puebla, W. J. Parak, J. Arbiol and A. Cabot, *J. Am. Chem. Soc.*, 2013, **135**, 7098-7101.
44. A. W. Jansons, L. K. Plummer and J. E. Hutchison, *Chem. Mater.*, 2017, **29**, 5415-5425.
45. A. W. Jansons and J. E. Hutchison, *ACS Nano*, 2016, **10**, 6942-6951.
46. J. Kim, G. K. Ong, Y. Wang, G. LeBlanc, T. E. Williams, T. M. Mattox, B. A. Helms and D. J. Milliron, *Nano Lett.*, 2015, **15**, 5574-5579.
47. S. Heo, J. Kim, G. K. Ong and D. J. Milliron, *Nano Lett.*, 2017, **17**, 5756-5761.
48. W. W. Yu, Y. A. Wang and X. Peng, *Chem. Mater.*, 2003, **15**, 4300-4308.
49. T. R. Gordon, M. Cargnello, T. Paik, F. Mangolini, R. T. Weber, P. Fornasiero and C. B. Murray, *J. Am. Chem. Soc.*, 2012, **134**, 6751-6761.
50. S. Ghosh, M. Saha, S. Paul and S. K. De, *Small*, 2017, **13**, 1602469-1602485.
51. R. Buonsanti, A. Llordes, S. Aloni, B. A. Helms and D. J. Milliron, *Nano Lett.*, 2011, **11**, 4706-4710.
52. Z. Zhang, X. Zhong, S. Liu, D. Li and M. Han, *Angew. Chem. Int. Ed.*, 2005, **44**, 3466-3470.
53. X. Zhong, Y. Feng, Y. Zhang, I. Lieberwirth and W. Knoll, *Small*, 2007, **3**, 1194-1199.
54. M.-R. Gao, Y.-F. Xu, J. Jiang and S.-H. Yu, *Chem. Soc. Rev.*, 2013, **42**, 2986-3017.
55. N. C. Anderson, M. P. Hendricks, J. J. Choi and J. S. Owen, *J. Am. Chem. Soc.*, 2013, **135**, 18536-18548.
56. F. Wang, Q. Li, L. Lin, H. Peng, Z. Liu and D. Xu, *J. Am. Chem. Soc.*, 2015, **137**, 12006-12012.
57. S. V. Kershaw, A. S. Susha and A. L. Rogach, *Chem. Soc. Rev.*, 2013, **42**, 3033-3087.
58. N. J. Kramer, K. S. Schramke and U. R. Kortshagen, *Nano Lett.*, 2015, **15**, 5597-5603.
59. L. Mangolini, E. Thimsen and U. Kortshagen, *Nano Lett.*, 2005, **5**, 655-659.
60. A. Alvarez Barragan, N. V. Ilawe, L. Zhong, B. M. Wong and L. Mangolini, *J. Phys. Chem. C*, 2017, **121**, 2316-2322.
61. A. W. Jansons, K. M. Koskela, B. M. Crockett and J. E. Hutchison, *Chem. Mater.*, 2017, **29**, 8167-8176.
62. D. Mocatta, G. Cohen, J. Schattner, O. Millo, E. Rabani and U. Banin, *Science*, 2011, **332**, 77.
63. R. G. Pearson, *J. Chem. Educ.*, 1968, **45**, 581-587.
64. R. G. Pearson, *J. Chem. Educ.*, 1968, **45**, 643-648.
65. E. Della Gaspera, A. S. R. Chesman, J. van Embden and J. J. Jasieniak, *ACS Nano*, 2014, **8**, 9154-9163.
66. O. Elimelech, J. Liu, A. M. Plonka, A. I. Frenkel and U. Banin, *Angew. Chem. Int. Ed.*, 2017, **56**, 10335-10340.
67. J. H. Hwang, D. D. Edwards, D. R. Kammler and T. O. Mason, *Solid State Ionics*, 2000, **129**, 135-144.
68. X. Ye, J. Fei, B. T. Diroll, T. Paik and C. B. Murray, *J. Am. Chem. Soc.*, 2014, **136**, 11680-11686.
69. H. Fang, M. Hegde, P. Yin, and P. V. Radovanovic, *Chem. Mater.,* 2017, **29**, 4970-4979.
70. P. Yin, Y. Tan, H. Fang, M. Hegde, and P. V. Radovanovic, *Nature Nanotech.,* 2018, **13**, 463-467.
71. K. H. Hartstein, A. M. Schimpf, M. Salvador, and D. R. Gamelin, *J. Phys. Chem. Lett.,* 2017, **8**, 1831-1836.
72. R. W. Johns, H. A. Bechtel, E. L. Runnerstrom, A. Agrawal, S. D. Lounis and D. J. Milliron, *Nat. Commun.*, 2016, **7**, 11583-11588.
73. B. T. Diroll, T. R. Gordon, E. A. Gaulding, D. R. Klein, T. Paik, H. J. Yun, E. D. Goodwin, D. Damodhar, C. R. Kagan and C. B. Murray, *Chem. Mater.*, 2014, **26**, 4579-4588.
74. I. Hamberg and C. G. Granqvist, *Appl. Phys. Lett.*, 1984, **44**, 721-723.
75. E. Gerlach, *J. Phys. C: Solid State Phys.*, 1986, **19**, 4585-4604.
76. H. Yin, Y. Kuwahara, K. Mori and H. Yamashita, *J. Mater. Chem. A*, 2018, **6**, 10932-10938.
77. Y. Kim, K. Y. Park, D. M. Jang, Y. M. Song, H. S. Kim, Y. J. Cho, Y. Myung and J. Park, *J. Phys. Chem. C*, 2010, **114**, 22141-22146.
78. J. Cui, Y. Li, L. Liu, L. Chen, J. Xu, J. Ma, G. Fang, E. Zhu, H. Wu, L. Zhao, L. Wang and Y. Huang, *Nano Lett.*, 2015, **15**, 6295-6301.
79. B. Tandon, G. S. Shanker and A. Nag, *J. Phys. Chem. Lett.*, 2014, **5**, 2306-2311.
80. B. Tandon, A. Yadav and A. Nag, *Chemistry of Materials*, 2016, **28**, 3620-3624.
81. J. Zhang, K. Tse, M. Wong, Y. Zhang and J. Zhu, *Front. Phys.*, 2016, **11**, 117405-117452.
82. S. Ghosh, M. Saha, V. Dev Ashok, B. Dalal and S. K. De, *J. Phys. Chem. C*, 2015, **119**, 1180-1187.
83. O. A. Balitskii, M. Sytnyk, J. Stangl, D. Primetzhofer, H. Groiss and W. Heiss, *ACS Appl. Mater. Interfaces*, 2014, **6**, 17770-17775.
84. G. M. Carroll, A. M. Schimpf, E. Y. Tsui and D. R. Gamelin, *J. Am. Chem. Soc.*, 2015, **137**, 11163-11169.
85. I. Kriegel, C. Urso, D. Viola, L. De Trizio, F. Scotognella, G. Cerullo and L. Manna, *J. Phys. Chem. Lett.*, 2016, **7**, 3873-3881.
86. C. N. Valdez, M. Braten, A. Soria, D. R. Gamelin and J. M. Mayer, *J. Am. Chem. Soc.*, 2013, **135**, 8492-8495.

87. N. Kinsey, M. Ferrera, V. M. Shalaev and A. Boltasseva, *J. Opt. Soc. Am. B*, 2015, **32**, 121-142.
88. G. Garcia, R. Buonsanti, E. L. Runnerstrom, R. J. Mendelsberg, A. Llordes, A. Anders, T. J. Richardson and D. J. Milliron, *Nano Lett.*, 2011, **11**, 4415-4420.
89. C. J. Dahlman, Y. Tan, M. A. Marcus and D. J. Milliron, *J. Am. Chem. Soc.*, 2015, **137**, 9160-9166.
90. A. Llordés, G. Garcia, J. Gazquez and D. J. Milliron, *Nature*, 2013, **500**, 323-326.
91. M. Hu, C. Novo, A. Funston, H. Wang, H. Staleva, S. Zou, P. Mulvaney, Y. Xia and G. V. Hartland, *J. Mater. Chem.*, 2008, **18**, 1949-1960.
92. V. Myroshnychenko, E. Carbó-Argibay, I. Pastoriza-Santos, J. Pérez-Juste, L. M. Liz-Marzán and F. J. García de Abajo, *Adv. Mater.*, 2008, **20**, 4288-4293.
93. K. L. Kelly, E. Coronado, L. L. Zhao and G. C. Schatz, *J. Phys. Chem. B*, 2003, **107**, 668-677.
94. S. Link and M. A. El-Sayed, *Annu. Rev. Phys. Chem.*, 2003, **54**, 331-366.
95. S. Balendhran, S. Walia, H. Nili, J. Z. Ou, S. Zhuiykov, R. B. Kaner, S. Sriram, M. Bhaskaran and K. Kalantar-zadeh, *Adv. Funct. Mater.*, 2013, **23**, 3952-3970.
96. T. Brezesinski, J. Wang, S. H. Tolbert and B. Dunn, *Nat. Mater.*, 2010, **9**, 146-151.
97. H.-S. Kim, J. B. Cook, H. Lin, Jesse S. Ko, Sarah H. Tolbert, V. Ozolins and B. Dunn, *Nat. Mater.*, 2016, **16**, 454-460.
98. H. Cheng, T. Kamegawa, K. Mori and H. Yamashita, *Angew. Chem. Int. Ed.*, 2014, **53**, 2910-2914.
99. M. Vasilopoulou, A. M. Douvas, D. G. Georgiadou, L. C. Palilis, S. Kennou, L. Sygellou, A. Soultati, I. Kostis, G. Papadimitropoulos, D. Davazoglou and P. Argitis, *J. Am. Chem. Soc.*, 2012, **134**, 16178-16187.
100. N. Li, Y. Li, G. Sun, Y. Zhou, S. Ji, H. Yao, X. Cao, S. Bao and P. Jin, *Nanoscale*, 2017, **9**, 8298-8304.
101. F. D. Hardcastle and I. E. Wachs, *J. Phys. Chem.*, 1991, **95**, 10763-10772.
102. Y. Li, J. Cheng, Y. Liu, P. Liu, W. Cao, T. He, R. Chen and Z. Tang, *J. Phys. Chem. C*, 2017, **121**, 5208-5214.
103. I. A. de Castro, R. S. Datta, J. Z. Ou, A. Castellanos-Gomez, S. Sriram, T. Daeneke and K. Kalantar-zadeh, *Adv. Mater.*, 2017, **29**, 1701619.
104. P. L. Baynton, H. Rawson and J. E. Stanworth, *Nature*, 1956, **178**, 910-911.
105. Q. Huang, S. Hu, J. Zhuang and X. Wang, *Chem. Eur. J.*, 2012, **18**, 15283-15287.
106. D. O. Scanlon, G. W. Watson, D. J. Payne, G. R. Atkinson, R. G. Egdell and D. S. L. Law, *J. Phys. Chem. C*, 2010, **114**, 4636-4645.
107. L. Q. Mai, B. Hu, W. Chen, Y. Y. Qi, C. S. Lao, R. S. Yang, Y. Dai and Z. L. Wang, *Adv. Mater.*, 2007, **19**, 3712-3716.
108. Z. Luo, R. Miao, T. D. Huan, I. M. Mosa, A. S. Poyraz, W. Zhong, J. E. Cloud, D. A. Kriz, S. Thanneeru, J. He, Y. Zhang, R. Ramprasad and S. L. Suib, *Adv. Energy Mater.*, 2016, **6**, 1600528-1600538.
109. T. Choksi and J. Greeley, *ACS Catal.*, 2016, **6**, 7260-7277.
110. M. M. Y. A. Alsaif, A. F. Chrimes, T. Daeneke, S. Balendhran, D. O. Bellisario, Y. Son, M. R. Field, W. Zhang, H. Nili, E. P. Nguyen, K. Latham, J. van Embden, M. S. Strano, J. Z. Ou and K. Kalantar-zadeh, *Adv. Funct. Mater.*, 2016, **26**, 91-100.
111. M. Onoda, K. Toriumi, Y. Matsuda and M. Sato, *J. Solid State Chem.*, 1987, **66**, 163-170.
112. O. Glemser and G. Lutz, *Naturwissenschaften*, 1950, **37**, 539-540.
113. M. M. Y. A. Alsaif, M. R. Field, T. Daeneke, A. F. Chrimes, W. Zhang, B. J. Carey, K. J. Berean, S. Walia, J. van Embden, B. Zhang, K. Latham, K. Kalantar-zadeh and J. Z. Ou, *ACS Appl. Mater. Interfaces*, 2016, **8**, 3482-3493.
114. M. M. Y. A. Alsaif, K. Latham, M. R. Field, D. D. Yao, N. V. Medehkar, G. A. Beane, R. B. Kaner, S. P. Russo, J. Z. Ou and K. Kalantar-zadeh, *Adv. Mater.*, 2014, **26**, 3931-3937.
115. X. K. Hu, Y. T. Qian, Z. T. Song, J. R. Huang, R. Cao and J. Q. Xiao, *Chem. Mater.*, 2008, **20**, 1527-1533.
116. B. Braïda, S. Adams and E. Canadell, *Chem. Mater.*, 2005, **17**, 5957-5969.
117. E. Canadell and M. H. Whangbo, *Chem. Rev.*, 1991, **91**, 965-1034.
118. M. Greenblatt, *Chem. Rev.*, 1988, **88**, 31-53.
119. P. G. Dickens, J. J. Birtill and C. J. Wright, *J. Solid State Chem.*, 1979, **28**, 185-193.
120. A. Agrawal, S. H. Cho, O. Zandi, S. Ghosh, R. W. Johns and D. J. Milliron, *Chem. Rev.*, 2018, **118**, 3121-3207.
121. X. Tan, L. Wang, C. Cheng, X. Yan, B. Shen and J. Zhang, *ChemComm.*, 2016, **52**, 2893-2896.
122. G. Zhang, T. Xiong, M. Yan, L. He, X. Liao, C. He, C. Yin, H. Zhang and L. Mai, *Nano Energy*, 2018, **49**, 555-563.
123. X. Zhou, H.-Y. Zhou, T.-Y. Cheang, Z.-W. Zhao, C.-C. Shen, K. Liang, Y.-N. Liu, Z.-K. Yang, M. Imran and A.-W. Xu, *J. Phys. Chem. C*, 2017, **121**, 27528-27534.
124. H. Cheng, X. Qian, Y. Kuwahara, K. Mori and H. Yamashita, *Adv. Mater.*, 2015, **27**, 4616-4621.
125. H. Cheng, M. Wen, X. Ma, Y. Kuwahara, K. Mori, Y. Dai, B. Huang and H. Yamashita, *J. Am. Chem. Soc.*, 2016, **138**, 9316-9324.
126. Y. Kuwahara, Y. Yoshimura, K. Haematsu and H. Yamashita, *J. Am. Chem. Soc.*, 2018, **140**, 9203-9210.
127. H. Yin, Y. Kuwahara, K. Mori, M. Che and H. Yamashita, *J. Mater. Chem. A*, 2019, **7**, 3783-3789.
128. H. Zhang, K.-W. Jeon and D.-K. Seo, *ACS Appl. Mater. Interfaces*, 2016, **8**, 21539-21544.
129. Z. Chen, D. Cummins, B. N. Reinecke, E. Clark, M. K. Sunkara and T. F. Jaramillo, *Nano Lett.*, 2011, **11**, 4168-4175.
130. H. Zheng, J. Z. Ou, M. S. Strano, R. B. Kaner, A. Mitchell and K. Kalantar-zadeh, *Adv. Funct. Mater.*, 2011, **21**, 2175-2196.
131. F. J. Castro, F. Tonus, J.-L. Bobet and G. Urretavizcaya, *J. Alloys Compd.*, 2010, **495**, 537-540.
132. M. A. Vannice, M. Boudart and J. J. Fripiat, *J. Catal.*, 1970, **17**, 359-365.
133. F. D. Hardcastle and I. E. Wachs, *J. Raman Spectrosc.*, 1995, **26**, 397-405.
134. M. F. Daniel, B. Desbat, J. C. Lassegues, B. Gerand and M. Figlarz, *J. Solid State Chem.*, 1987, **67**, 235-247.
135. T. M. Mattox, A. Bergerud, A. Agrawal and D. J. Milliron, *Chem. Mater.*, 2014, **26**, 1779-1784.
136. P. G. Dickens and M. S. Whittingham, *Q. Rev. Chem. Soc.*, 1968, **22**, 30-44.
137. Y. Lee, T. Lee, W. Jang and A. Soon, *Chem. Mater.*, 2016, **28**, 4528-4535.
138. M. J. Sienko and H. Oesterreicher, *J. Am. Chem. Soc.*, 1968, **90**, 6568-6570.
139. P. G. Dickens and R. J. Hurditch, *Nature*, 1967, **215**, 1266-1267.

140. G. Wang, Y. Ling, H. Wang, X. Yang, C. Wang, J. Z. Zhang and Y. Li, *Energy Environ. Sci.*, 2012, **5**, 6180-6187.
141. J. Song, Z.-F. Huang, L. Pan, J.-J. Zou, X. Zhang and L. Wang, *ACS Catal.*, 2015, **5**, 6594-6599.
142. Y. Li, Z. Tang, J. Zhang and Z. Zhang, *J. Phys. Chem. C*, 2016, **120**, 9750-9763.
143. T. Paik, M. Cargnello, T. R. Gordon, S. Zhang, H. Yun, J. D. Lee, H. Y. Woo, S. J. Oh, C. R. Kagan, P. Fornasiero and C. B. Murray, *ACS Energy Lett.*, 2018, **3**, 1904-1910.
144. Z. Lou, Q. Gu, Y. Liao, S. Yu and C. Xue, *Appl. Catal. B-Environ.*, 2016, **184**, 258-263.
145. A. K. Shukla, M. K. Ravikumar, S. Aricò, G. Candiano, V. Antonucci, N. Giordano and A. Hamnett, *J. Appl. Electrochem.*, 1995, **25**, 528-532.
146. N. Xue, R.-J. Yu, C.-Z. Yuan, X. Xie, Y.-F. Jiang, H.-Y. Zhou, T.-Y. Cheang and A.-W. Xu, *RSC Adv.*, 2017, **7**, 2351-2357.
147. J. Huang, D. Ma, F. Chen, D. Chen, M. Bai, K. Xu and Y. Zhao, *ACS Appl. Mater. Interfaces*, 2017, **9**, 7436-7446.
148. A. B. Yousaf, M. Imran, S. J. Zaidi and P. Kasak, *Sci. Rep.*, 2017, **7**, 6574-6584.
149. L. Changhai, Q. Yangyang, X. Yujian, W. Fang, L. Xiaocun, S. Xuhui, L. Qian and C. Zhidong, *Nanotechnology*, 2017, **28**, 445403-445413.
150. K. Yuan, Q. Cao, H.-L. Lu, M. Zhong, X. Zheng, H.-Y. Chen, T. Wang, J.-J. Delaunay, W. Luo, L. Zhang, Y.-Y. Wang, Y. Deng, S.-J. Ding and D. W. Zhang, *J. Mater. Chem. A*, 2017, **5**, 14697-14706.
151. X. C. Song, E. Yang, G. Liu, Y. Zhang, Z. S. Liu, H. F. Chen and Y. Wang, *J. Nanoparticle Res.*, 2010, **12**, 2813-2819.
152. H. Yin, Y. Kuwahara, K. Mori, H. Cheng, M. Wen, Y. Huo and H. Yamashita, *J. Phys. Chem. C*, 2017, **121**, 23531-23540.
153. N. Zhang, A. Jalil, D. Wu, S. Chen, Y. Liu, C. Gao, W. Ye, Z. Qi, H. Ju, C. Wang, X. Wu, L. Song, J. Zhu and Y. Xiong, *J. Am. Chem. Soc.*, 2018, **140**, 9434-9443.

TOC Graphic:

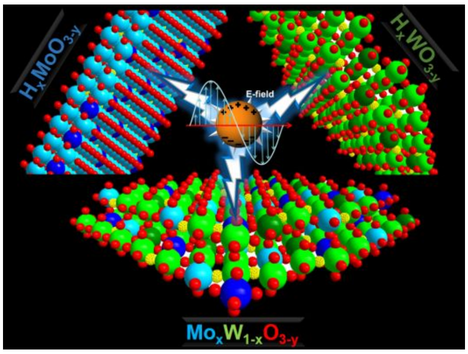

We highlight the three widely explored oxide-based plasmonic materials, including H_xMoO_{3-y}, H_xWO_{3-y}, and $Mo_xW_{1-x}O_{3-y}$ and their applications in catalysis.